Small and large deformation analysis with the *p*- and B-spline versions of the Finite Cell Method

**Dominik Schillinger · Martin Ruess · Nils Zander ·
Yuri Bazilevs · Alexander Düster · Ernst Rank**

Abstract The Finite Cell Method (FCM) is an embedded domain method, which combines the fictitious domain approach with high-order finite elements, adaptive integration, and weak imposition of unfitted Dirichlet boundary conditions. For smooth problems, FCM has been shown to achieve exponential rates of convergence in energy norm, while its structured cell grid guarantees simple mesh generation irrespective of the geometric complexity involved. The present contribution first unhinges the FCM concept from a special high-order basis. Several benchmarks of linear elasticity and a complex proximal femur bone with inhomogeneous material demonstrate that for small deformation analysis, FCM works equally well with basis functions of the *p*-version of the finite element method or high-order B-splines. Turning to large deformation analysis, it is then illustrated that a straightforward geometrically nonlinear FCM formulation leads to the loss of uniqueness of the deformation map in the fictitious domain. Therefore, a modified FCM formulation is introduced, based on repeated deformation resetting, which assumes for the fictitious domain the deformation-free reference configuration after each Newton iteration. Numerical experiments show that this intervention allows for stable nonlinear FCM analysis, preserving the full range of advantages of linear elastic FCM, in particular exponential rates of convergence. Finally, the weak imposition of unfitted Dirichlet boundary conditions via the penalty method, the robustness of FCM under severe mesh distortion, and the large deformation analysis of a complex voxel-based metal foam are addressed.

Keywords Embedded domain methods · Immersed boundary methods · Fictitious domain methods · *p*-Version of the Finite Cell Method · B-spline version of the Finite Cell Method · Large deformation solid mechanics · Weak boundary conditions

D. Schillinger (✉) · M. Ruess · N. Zander · E. Rank
Lehrstuhl für Computation in Engineering, Department of Civil Engineering and Surveying, Technische Universität München, Arcisstr. 21, 80333 Munich, Germany
e-mail: schillinger@bv.tum.de

M. Ruess
e-mail: ruess@bv.tum.de

N. Zander
e-mail: zander@bv.tum.de

E. Rank
e-mail: rank@bv.tum.de

Y. Bazilevs
Department of Structural Engineering, University of California, San Diego, 9500 Gilman Drive, La Jolla, CA, USA
e-mail: yuri@ucsd.edu

A. Düster
Numerische Strukturanalyse mit Anwendungen in der Schiffstechnik (M-10), Technische Universität Hamburg-Harburg, Schwarzenbergstr. 95c, 21073 Hamburg, Germany
e-mail: alexander.duester@tu-harburg.de

1 Introduction

Structural analysis with standard finite elements requires the discretization of the domain of interest into a finite element mesh, whose boundaries conform to the physical boundaries of the structure [1,2]. While this constraint can be easily achieved for many applications in solid mechanics, it constitutes a severe bottleneck for structures of highly complex geometry. The meshing challenge has recently led to the rise of isogeometric methods, which directly use the spline basis of a CAD model for FE analysis (see [3–5] and the references therein). A more general approach to avoid time-consuming mesh generation for complex domains is provided by embedded domain methods, also known as

immersed boundary methods [6–9], in conjunction with the fictitious domain concept [10–12]. The main idea consists of the extension of the physical domain of interest Ω_{phys} beyond its potentially complex boundaries into a larger embedding domain of simple geometry Ω, which can be meshed easily by a structured grid (see Fig. 1). To preserve consistency with the original problem, the influence of the fictitious domain extension Ω_{fict} is extinguished by penalizing its material parameters. The fictitious domain approach has been widely used in conjunction with penalty methods [12,13], the mortar approach [14], Lagrange multipliers [11,15–18], Nitsche's method [19], extended finite elements [20–23], discontinuous Galerkin [24] and spectral methods [25–27] to address problems of structural analysis, acoustics, fluid and heat flow, fluid-structure interaction, topology and shape optimization.

The Finite Cell Method (FCM) [28,29] is an embedded domain method, which combines the fictitious domain approach of Fig. 1 with the p-version of the finite element method (FEM) [30,31], adaptive integration and weak imposition of unfitted Dirichlet boundary conditions. For smooth problems of linear elasticity, FCM has been shown to maintain exponential rates of convergence in energy norm known from the p-version. FCM thus allows for accurate structural analysis irrespective of the geometric complexity involved [32], and can be well combined with voxel-based geometrical models typical for applications from biomechanics and material science [29,33,34]. Within the framework of FCM, the following aspects have been examined so far: Fluid-structure interaction [35], topology optimization [36], thin-walled structures [37], local refinement strategies [34], weak boundary conditions [33,38,39], elasto-plasticity [40], advection-diffusion problems [41], homogenization of porous and cellular materials [42], and computational steering [43]. In this context, the present contribution brings in two main new aspects: first, the application of high-order and high-continuity B-spline bases within the generalized Finite Cell concept, coined the B-spline version of the FCM, and second, the extension of the FCM concept to geometrically nonlinear problems based on deformation resetting.

The article at hand is organized as follows: Sect. 2 provides a generalized presentation of the Finite Cell concept as well as the p- and B-spline versions, highlighting the different derivation and characteristics of their high-order

bases. Using linear elastic problems first, Sect. 3 demonstrates the equivalent solution behavior of the p- and B-spline versions of the FCM in conjunction with Nitsche's method and for a complex three-dimensional proximal femur bone with inhomogeneous material. Turning to geometrically nonlinear problems, Sect. 4 introduces a FCM formulation based on the logarithmic strain measure. Section 5 demonstrates that a standard FCM approach applying the same kinematics over the complete domain leads to the loss of uniqueness of the nonlinear deformation map within the fictitious domain. It motivates its modification by the idea of deformation resetting, which assumes the initial reference configuration within Ω_{fict} after each Newton iteration. Section 6 provides a geometrically nonlinear formulation of the penalty method for the imposition of unfitted Dirichlet constraints in elements cut by the geometric boundary. Section 7 presents a range of numerical benchmarks, which demonstrate stability, accuracy, physical consistency and exponential rates of convergence for the modified geometrically nonlinear FCM formulation applied within the p- and B-spline versions. Section 8 addresses its behavior under severe mesh distortion, which is fundamental for the representation of very large deformation states. Section 9 presents an application oriented large deformation analysis of a complex metal foam sample, demonstrating the capability of FCM to directly operate on voxel-based geometrical models. Sections 10 and 11 terminate the present study, giving a comparison of the p- and B-spline versions as well as some conclusions.

2 The Finite Cell Method with high-order p-version and B-spline bases

Following a brief review of the Finite Cell concept, the integration of the p-version and B-spline bases into the FCM framework is discussed. The resulting two FCM schemes are referred to as the p- and B-spline versions of the FCM in the following.

2.1 The fictitious domain concept

As shown in Fig. 1, the embedding domain Ω consists of the physical domain of interest Ω_{phys} and the fictitious domain
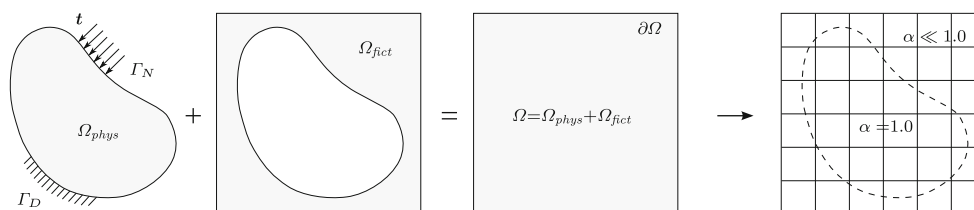

Fig. 1 The fictitious domain concept: the physical domain Ω_{phys} is extended by the fictitious domain Ω_{fict} into an embedding domain Ω to allow easy meshing of complex geometries. The influence of Ω_{fict} is penalized by α
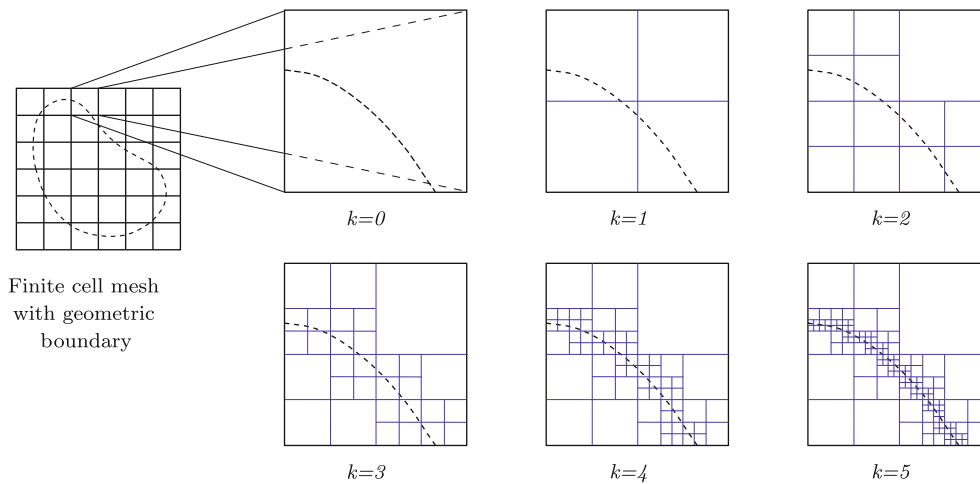
Fig. 2 2D sub-cell structure (*thin blue lines*) for adaptive integration of finite cells (*bold black lines*) cut by the geometric boundary (*dashed line*). (color figure online)

extension Ω_{fict}. Analogous to standard FEM, the FCM for linear elastic problems is derived from the principle of virtual work

$$\delta W (\boldsymbol{u}, \delta \boldsymbol{u}) = \int_{\Omega} \boldsymbol{\sigma} : (\nabla_{sym} \delta \boldsymbol{u}) \, dV - \int_{\Omega_{phys}} \delta \boldsymbol{u} \cdot \boldsymbol{b} \, dV$$

$$- \int_{\Gamma_N} \delta \boldsymbol{u} \cdot \boldsymbol{t} \, dA = 0 \qquad (1)$$

where $\boldsymbol{\sigma}$, $\boldsymbol{b}$, $\boldsymbol{u}$, $\delta \boldsymbol{u}$ and ∇_{sym} denote the Cauchy stress tensor, body forces, displacement vector, test function and the symmetric part of the gradient, respectively [1,2]. Neumann boundary conditions are specified over the boundary of the embedding domain $\partial \Omega$, where tractions are zero by definition, and over Γ_N of the physical domain by traction vector $\boldsymbol{t}$ (see Fig. 1). The elasticity tensor $\boldsymbol{C}$ [1,2] relating stresses and strains

$$\boldsymbol{\sigma} = \alpha \boldsymbol{C} : \boldsymbol{\varepsilon} \qquad (2)$$

is complemented by a scalar factor α, which leaves the material parameters unchanged in the physical domain, but penalizes the contribution of the fictitious domain

$$\alpha (\boldsymbol{x}) = \begin{cases} 1.0 & \forall \boldsymbol{x} \in \Omega_{phys} \\ 10^{-q} & \forall \boldsymbol{x} \in \Omega_{fict} \end{cases} \qquad (3)$$

In Ω_{fict}, α must be chosen as small as possible, but large enough to prevent extreme ill-conditioning of the stiffness matrix [28,29]. Typical values of α range between 10^{-4} and 10^{-15}. The idea of applying a penalized material for void regions of a domain has also been frequently used in optimization, see for example [6,44].

Using a structured grid of high-order elements (see Fig. 1), which will be called finite cells in the following, kinematic quantities are discretized as

$$\boldsymbol{u} = \sum_{a=1}^{n} N_a \boldsymbol{u}_a \qquad (4)$$

$$\delta \boldsymbol{u} = \sum_{a=1}^{n} N_a \delta \boldsymbol{u}_a \qquad (5)$$

The sum of N_a denotes a finite set of n high-order shape functions, and $\boldsymbol{u}_a$ and $\delta \boldsymbol{u}_a$ the corresponding vectors of unknown coefficients [2,45]. Following the standard Bubnov-Galerkin approach [1,2], inserting Eqs. 4 and 5 into the weak form Eq. 1 produces a discrete finite cell representation

$$\boldsymbol{K}\boldsymbol{u} = \boldsymbol{f} \qquad (6)$$

with stiffness matrix $\boldsymbol{K}$ and load vector $\boldsymbol{f}$. Due to the similarity to standard FEM, the implementation of FCM can exploit existing finite element techniques to the full.

2.2 Adaptive integration

The accuracy of numerical integration by Gauss quadrature [2,46], which assumes smoothness of the integrands, is considerably influenced by discontinuities within cells introduced by the penalization parameter α of Eq. 3 [28,29]. Therefore, the FCM uses composed Gauss quadrature to improve integration accuracy in cells cut by geometric boundaries, based on a hierarchical decomposition of the original cell into integration sub-cells [29]. In two dimensions, the sub-cell structure can be built up in the sense of a quadtree (see Fig. 2) [47]. Starting from the original finite cell of level $k = 0$, each sub-cell of level $k = i$ is first checked whether it is cut by a geometric boundary. If true, it is replaced by 4 equally spaced cells of level $k = i + 1$, each of which is equipped with $(p + 1) \times (p + 1)$ Gauss points. Partitioning is repeated for all cells of current level k, until

a predefined maximum depth $k = m$ is reached. The quad-tree approach can be easily adjusted to 1D or 3D by binary trees or octrees, respectively [29,47]. To clearly distinguish between finite cell and sub-cell meshes, finite cells are plotted in black and integration sub-cells are plotted in blue lines throughout this paper (see Fig. 2).

The adaptive integration scheme is easy to implement, keeps the regular grid structure of FCM, and requires considerably less computational effort than non-adaptive schemes such as the Gauss point method [28,48]. However, the major part of the computational cost of the FCM still stems from linear algebra operations, which need to be repeated many times due to the large number of Gauss points in the sub-cell structure during integration of the stiffness matrix. Note that a reduction of the $(p+1)$ Gauss points in each sub-cell direction is not recommended, since this introduces an additional integration error, which for instance dramatically decreases the convergence rate of the Newton–Raphson procedure or can provoke a random failure of the nonlinear deformation mapping.

2.3 The p-version of the FCM

The high-order basis originally applied in the FCM [28,29] uses a regular mesh of elements of the p-version of the FEM, introduced by Szabó and Babuška [30,31,49,50]. Its formulation is based on integrated Legendre polynomials of the form

$$
\begin{aligned}
\phi_j(\xi) &= \sqrt{\frac{2j-1}{2}} \int_{-1}^{\xi} P_{j-1}(t)dt \\
&= \frac{1}{\sqrt{4j-2}} \left(P_j(\xi) - P_{j-2}(\xi) \right), \quad j = 2, 3, \ldots \quad (7)
\end{aligned}
$$

where $P_j(\xi)$ are standard Legendre polynomials in local cell coordinates [30,46]. As illustrated in Fig. 3, the one-dimensional basis is constructed by combining the standard linear shape functions with higher-order functions provided by Eq. 7. The basis is hierarchic, so that an increase of the polynomial degree p of the basis by 1 is achieved by the addition of another ϕ_j [30,49].

Corresponding higher-dimensional bases can be constructed by tensor products of the 1D case. 2D shape functions are usually grouped as follows (see Fig. 4):

– *Nodal modes* are the standard bilinear shape functions [1,2,30]. The corresponding mode for node n_1 of Fig. 4 reads

$$
N_1^{n_1}(\xi, \eta) = \frac{1}{4}(1 - \xi)(1 - \eta) \quad (8)
$$

– *Edge modes* are defined separately for each individual edge and vanish at all other edges. The corresponding modes for edge e_1 of Fig. 4 read
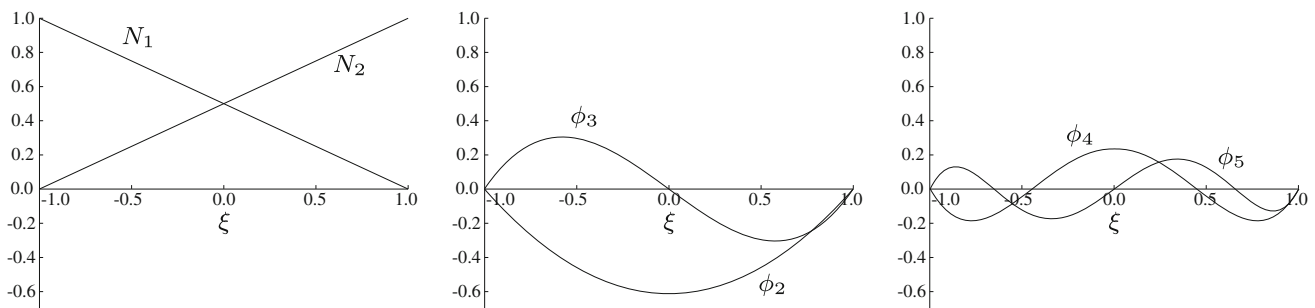

Fig. 3 Linear nodal modes N_j, $j = 1, 2$ and the first four integrated Legendre basis functions ϕ_j, $j = 2, \ldots, 5$ of the 1D p-version basis in the parameter space ξ. Their combination yields the shape functions of a 1D finite cell of $p = 5$

Nodal mode $N_1^{n_1}$ at node n_1 Quadratic edge mode $N_2^{e_1}$ at edge e_1 Quadratic internal mode $N_{2,2}^{int}$
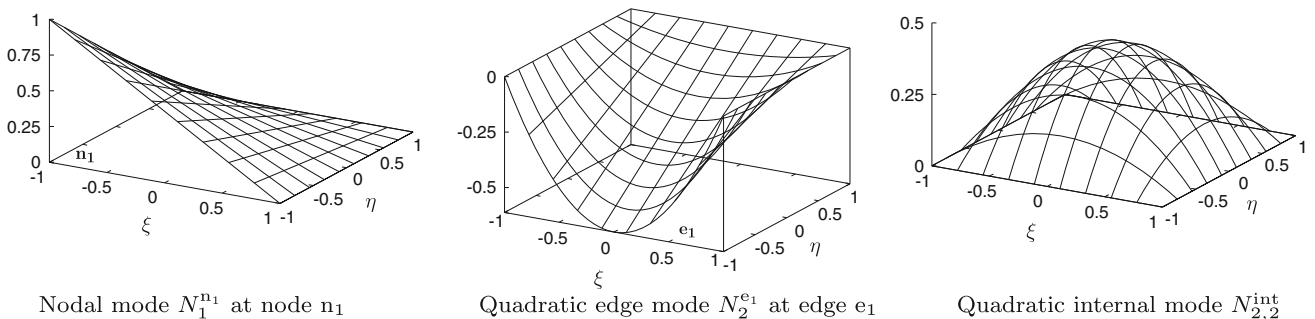
Fig. 4 Examples of shape functions of the 2D p-version basis in the parameter space $[\xi, \eta]$

Fig. 5 Example of an open cubic B-spline patch consisting of three uniform B-splines and six knot spans. At the boundaries, knots are repeated four times to obtain interpolatory B-splines
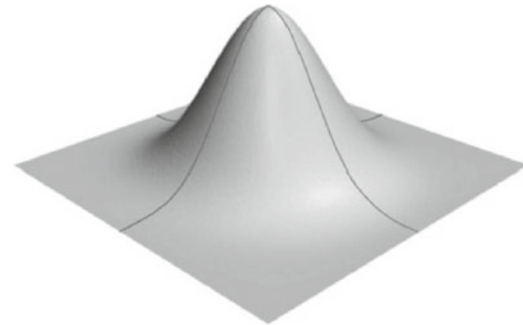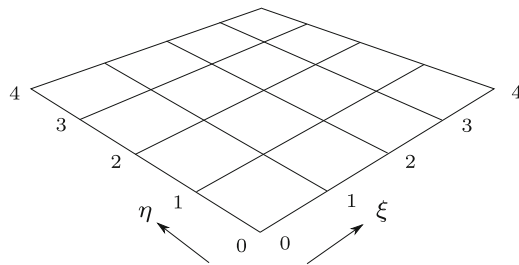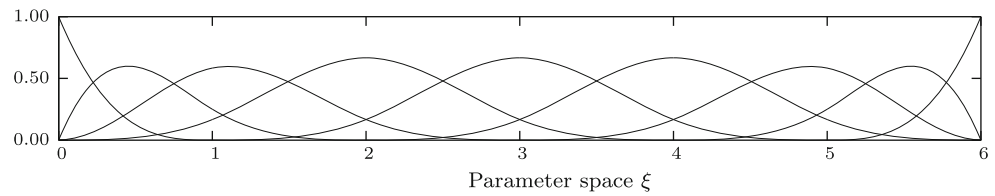

Fig. 6 Knot span cells in the parameter space $\{\xi, \eta\}$ (*left*) and corresponding bi-variate cubic B-spline (*right*)

$$N_i^{e_1}(\xi, \eta) = \frac{1}{2}(1 - \eta)\phi_i(\xi) \tag{9}$$

– *Internal modes* are purely local and vanish at all element edges. They read

$$N_{i,j}^{int}(\xi, \eta) = \phi_i(\xi)\phi_j(\eta) \tag{10}$$

For the three-dimensional basis, see [30,31,49,50]. To limit the number of additional unknowns in 2D and 3D, the so-called *trunk space* is used instead of the full tensor product basis [31,49].

The geometry of the structured finite cell mesh in terms of the position vector X can be represented exactly by the nodal part alone

$$X = \sum_{i=1}^{n_{vert}} N_i^n X_i \tag{11}$$

where X_i and N_i^n denote the location of the n_{vert} cell vertices and the corresponding nodal modes, respectively. The p-version of the FCM can thus be regarded as a sub-parametric finite element scheme [1]. The resulting FCM stiffness matrix Eq. 6 inherits all beneficial properties of the p-version FEM, such as hierarchy of the modal contributions and a tremendous improvement of the condition number under p-refinement with respect to standard nodal FE schemes [30,31,49].

2.4 The B-spline version of the FCM

The B-spline version of the FCM has been recently established as a suitable alternative [51,52]. Its formulation is based on high-order B-spline basis functions $N_{i,p}$ of polynomial degree p, which are defined by $p + 2$ knots $\xi_1 \leq \xi_2 \leq$ $\cdots \leq \xi_{p+2}$ in the parameter space ξ [3,4]. The resulting $p + 1$ knot spans contain piecewise polynomials of degree p, which join smoothly up to a continuous differentiability of C^{p-1} [53,54]. A number of n basis functions constitute a patch, defined by a so-called knot vector [4,53,54]

$$\Xi = \{\xi_1, \xi_2, \ldots, \xi_{n+p+1}\}, \quad \xi_1 \leq \xi_2 \leq \cdots \leq \xi_{n+p+1} \tag{12}$$

The knots of each individual basis function $N_{i,p}$ with patch index i can be identified as the consecutive entries $\{i, i + 1, \ldots, i + p + 1\}$ in Ξ. B-spline basis functions $N_{i,p}$ of arbitrary polynomial degree p can be generated recursively with the Cox-de Boor formula, starting from piecewise constants $N_{i,0}$ [53,54]

$$N_{i,0}(\xi) = \begin{cases} 1, & \text{if } \xi_i \leq \xi \leq \xi_{i+1} \\ 0, & \text{otherwise} \end{cases} \tag{13}$$

$$N_{i,p}(\xi) = \frac{\xi - \xi_i}{\xi_{i+p} - \xi_i} N_{i,p-1}(\xi)$$
$$+ \frac{\xi_{i+p+1} - \xi}{\xi_{i+p+1} - \xi_{i+1}} N_{i+1,p-1}(\xi) \tag{14}$$

A uniform B-spline patch with open knot vectors as illustrated in Fig. 5 guarantees optimal approximation for smooth problems due to maximum continuity within the patch, but also allows for the imposition of boundary conditions by standard FE techniques [3,4]. Its basis functions away from the boundary of the patch consist of uniform B-splines constructed from equidistant knots, which can be interpreted as translated copies of each other [55]. At the boundaries, knots are repeated $p + 1$ times in order to make the basis interpolatory.

The two-dimensional B-spline basis uses two independent 1D open knot vectors with indices $\{i, j\}$ for local coordinates $\{\xi, \eta\}$, respectively. The parameter space is then discretized
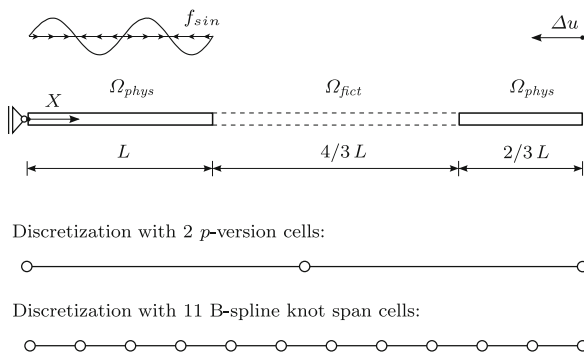
Fig. 7 Uni-axial rod example. Geometric boundaries are located at $X = 1.0$ and $X = 2\frac{1}{3}$. Parameters: Young's modulus $E = 1.0$; Poisson's ratio $\nu = 0.0$; penalization parameter $\alpha = 10^{-q}$; area $A = 1.0$; length of each part $L = 1.0$; displacement load $\Delta u = 0.02$; Sine load $f_{\sin} = 1/20 \sin(4\pi X)$

by a structured grid of knot spans, whose nodal positions can be obtained by permuting all entries $\{i, j\}$. Corresponding multivariate B-spline basis functions are obtained by taking the tensor product of its univariate components

$$N_{i,j,p}(\xi, \eta) = N_{i,p}(\xi) \cdot N_{j,p}(\eta) \qquad (15)$$

An example of two-dimensional knot spans and a corresponding bi-cubic uniform B-spline are shown in Fig. 6. The three-dimensional B-spline basis can be constructed analogously (see for example [3,52,55]).

In the framework of the FCM, the discretization is accomplished with a regular grid of knot spans of width h in the sense of the fictitious domain concept as illustrated in Fig. 1. In two and three dimensions, each knot span can be identified as a quadrilateral or hexahedral finite cell, respectively, with full Gaussian integration [51,52]. The physical coordinates X of the finite cell grid can be generated from a simple linear transformation of the parameter space $\boldsymbol{\xi}$

$$X = X_0 + h\,\boldsymbol{\xi} \qquad (16)$$

where X_0 denotes the origin of the physical coordinate system in the parameter space. The B-spline version of the FCM is thus also a sub-parametric scheme [1].

2.5 Weak imposition of unfitted Dirichlet constraints

In case of cuboidal domains, where boundaries coincide with cell boundaries of the structured grid, Dirichlet boundary conditions can be implemented strongly by standard FE techniques in both FCM versions [4,31]. In case of more complex domains, Dirichlet constraints are defined along boundaries of arbitrary geometry cutting through finite cells, which require an imposition in a weak sense by variational techniques such as the penalty method [56–58], the Lagrange multiplier method [11,21,59,60] or Nitsche's

method [61–64]. In the framework of FCM, Nitsche's method is usually preferred [33,39], since it does not introduce additional unknowns, leads to a symmetric, positive definite stiffness matrix and satisfies variational consistency in the sense that solutions of the weak form can be shown to be solutions of the original boundary value problem. In linear elasticity, Nitsche's method extends the weak form of Eq. 1 by additional terms as follows

$$\delta W_K(\boldsymbol{u}, \delta\boldsymbol{u}) = \int_\Omega \boldsymbol{\sigma} : (\nabla_{sym}\,\delta\boldsymbol{u})dV + \beta \int_{\Gamma_D} \boldsymbol{u} \cdot \delta\boldsymbol{u}\,dA$$
$$- \int_{\Gamma_D} \delta(\boldsymbol{\sigma} \cdot \boldsymbol{n}) \cdot \boldsymbol{u}\,dA - \int_{\Gamma_D} (\boldsymbol{\sigma} \cdot \boldsymbol{n}) \cdot \delta\boldsymbol{u}\,dA \qquad (17)$$

$$\delta W_f(\boldsymbol{u}, \delta\boldsymbol{u}) = \int_{\Omega_{phys}} \delta\boldsymbol{u} \cdot \boldsymbol{b}\,dV + \int_{\Gamma_N} \delta\boldsymbol{u} \cdot \boldsymbol{t}\,dA$$
$$+ \beta \int_{\Gamma_D} \hat{\boldsymbol{u}} \cdot \delta\boldsymbol{u}\,dA - \int_{\Gamma_D} \delta(\boldsymbol{\sigma} \cdot \boldsymbol{n}) \cdot \hat{\boldsymbol{u}}\,dA \qquad (18)$$

where $\delta W_K = \delta W_f$. Function $\hat{\boldsymbol{u}}$ denotes the prescribed displacements along the Dirichlet boundary Γ_D, scalar β is a stabilization parameter, which can be chosen empirically or according to a generalized Eigenvalue problem [59,63], and $\boldsymbol{n}$ is the outward unit normal vector on Γ_D. Evaluation of Eqs. 17 and 18 leads to the stiffness matrix $\boldsymbol{K}$ and the force vector $\boldsymbol{f}$, respectively, that form the discrete system of Eq. 6.

3 Numerical examples at small strains

Several examples of linear elasticity are presented in the following to demonstrate the equivalent overall characteristics of the p- and B-spline versions of the FCM for small deformation analysis.

3.1 Characteristic solution behavior: smooth extension of solution fields and exponential convergence

In the FCM, the polynomial degree p of the shape functions is increased to reduce the approximation error, while the structured high-order mesh remains unchanged. For the illustration of the typical solution behavior, a linear elastic uni-axial rod is examined, for which geometry, material and boundary conditions are specified in Fig. 7. Its middle part represents the fictitious domain Ω_{fict}, whose Young's modulus E is penalized with parameter $\alpha = 10^{-8}$. The example approximates the situation of two separate rods. The right one undergoes a rigid body movement Δu and the left one is subjected to a sine load $f_{\sin}$. The FCM discretizations considered consist of 2 p-version finite cells and 11 knot span cells as shown in Fig. 7. Due to the different construction of the bases, the B-spline version requires a denser knot span
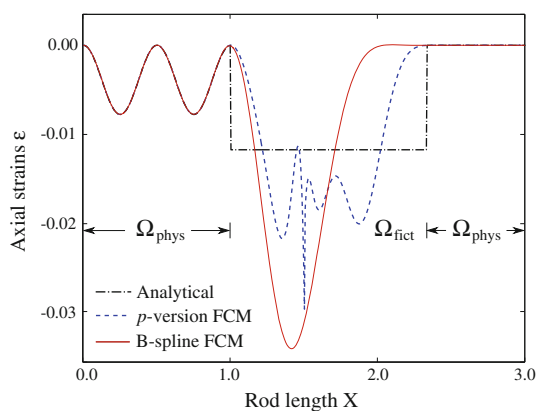
Fig. 8 Smooth extension of the FCM solutions ($p = 15$) versus discontinuous analytical solution ($\alpha = 10^{-8}$) for the linear elastic strains of the 1D example
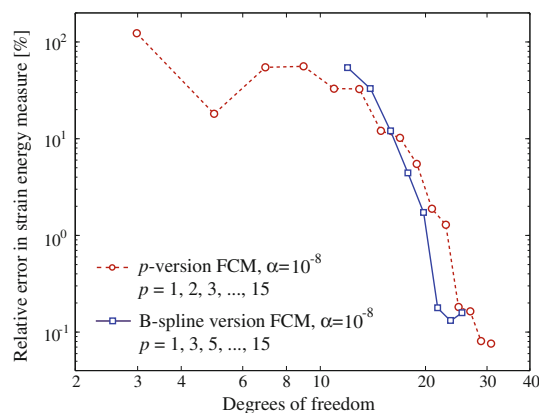

Fig. 9 Convergence in strain energy obtained by p-refinement in the given p-version and B-spline discretizations of the linear elastic 1D example

grid than the p-version in order to achieve a comparable amount of degrees of freedom (dofs). For all computations of this section, adaptive sub-cells of depth $k = 20$ are used to minimize the integration error in cells cut by geometric boundaries (see Sect. 2.2).

The corresponding analytical solution fields with finite $\alpha = 10^{-8}$ exhibit kinks and jumps in displacements and strains, respectively, at geometric boundaries $X = L$ and $X = 7/3L$. The analytical solution is approximated by an overkill solution with 1,800 equally-spaced standard cubic finite elements, where the geometric boundaries coincide with nodes, so that discontinuities can be represented. The p- and B-spline versions of the FCM, however, produce solution fields, which extend smoothly into the fictitious domain despite the discontinuities of the analytical solution. This is illustrated in Fig. 8, which compares the analytical strains to the numerical strains of the p- and B-spline versions. The importance of the smooth extension of the FCM solution into the fictitious domain for the overall convergence behavior of the FCM can be explained with the help of the penalty parameter α in conjunction with the total strain energy

$$U = \int_{\Omega} \Psi \, dV = \frac{1}{2} \int_{\Omega} \boldsymbol{\sigma} : \boldsymbol{\varepsilon} \, dV \qquad (19)$$

where Ψ represents the strain energy function, defined over the complete domain Ω. The best approximation property to the total strain energy U states that the solution of a Galerkin finite element scheme represents a least-squares best fit to the exact solution in terms of Eq. 19 [2,60]. Due to the penalization with parameter α of Eq. 3, deviations from the exact solution in Ω_{fict} have a considerably smaller impact on the strain energy Eq. 19 than deviations in Ω_{phys}. Therefore, a minimization of the strain energy error by the high-order basis of the FCM scheme results in an accurate approximation in Ω_{phys}, where potential deviations

lead to considerable error contributions. In Ω_{fict}, a largely inaccurate approximation is allowed, since potential deviations lead to negligible error contributions due to penalization. In particular, this implies a smooth extension of the solution into the fictitious domain, so that its gradients in Ω_{phys} remain unaffected up to the geometric boundary (see Fig. 8).

Accuracy and convergence of the FCM versions will be assessed by

$$e_r = \sqrt{\frac{|U_{ex} - U_{FCM}|}{U_{ex}}} \times 100\% \qquad (20)$$

denoting the relative error in terms of the total strain energy U of Eq. 19 [2,31,60]. U_{ex} represents the exact strain energy of the original problem defined over the physical domain Ω_{phys}. Accordingly, U_{FCM} denotes the strain energy contribution from Ω_{phys}, obtained numerically with an FCM scheme. The corresponding rate of convergence q, with which e_r decreases from the ith to the $(i + 1)$th p-refinement step compared to the number of degrees of freedom n_{dof} is

$$q = -\frac{\log_{10}\left(e_r^{i+1}/e_r^i\right)}{\log_{10}\left(n_{dof}^{i+1}/n_{dof}^i\right)} \qquad (21)$$

The physical reference strain energy U_{ex} for the example of Fig. 7 consists of the energy contribution by f_{sin} only. An overkill discretization with 1,000 cubic finite elements taking into account the left rod only yields $U_{ex} = 1.1873576208 \times 10^{-5}$. Figure 9 shows the convergence behavior of the presented FCM schemes, if the polynomial degree of the discretizations given in Fig. 7 is increased from $p = 1$–15. Both the p-version and the B-spline version of the FCM converge exponentially with a maximum rate of $q = 23.56$ and $q = 23.74$, respectively. The penalization parameter $\alpha = 10^{-8}$ cannot completely erase the influence of the fictitious domain, and the corresponding error takes control at a value

Fig. 10 Ring under internal radial pressure and fixed outer displacements. Parameters: $\Gamma_1 : \hat{u} = [0.0 0.0]^T$, $\Gamma_2 :$ $\hat{t} = \frac{1}{2} \frac{\ln 0.25 + 1}{\ln 2}$; $r_{in} = 0.25$; $r_{out} = 1.0$; $\Omega_{phys} : E_{phys} = 1.0$; $\Omega_{fict} = \alpha \cdot E_{phys}$; $\alpha = 10^{-15}$; $\nu = 0.0$
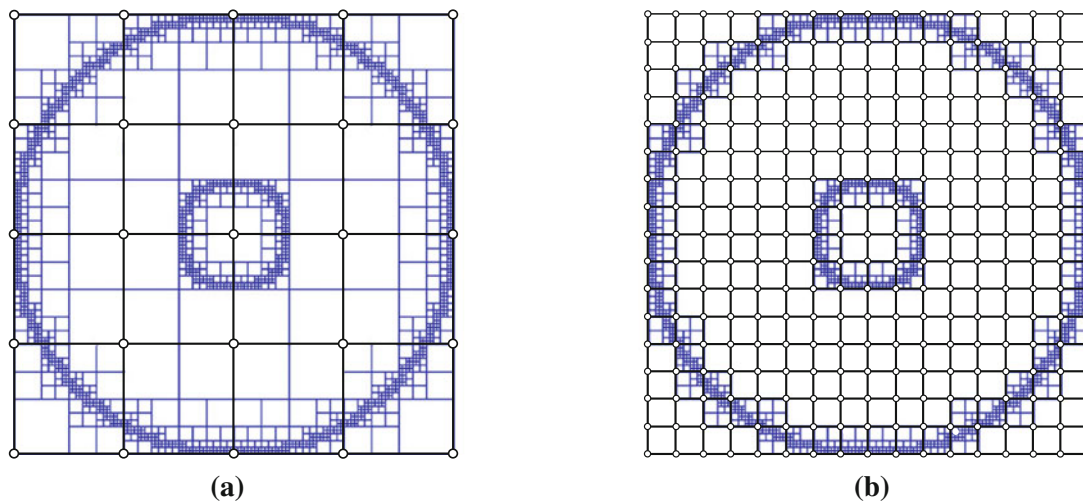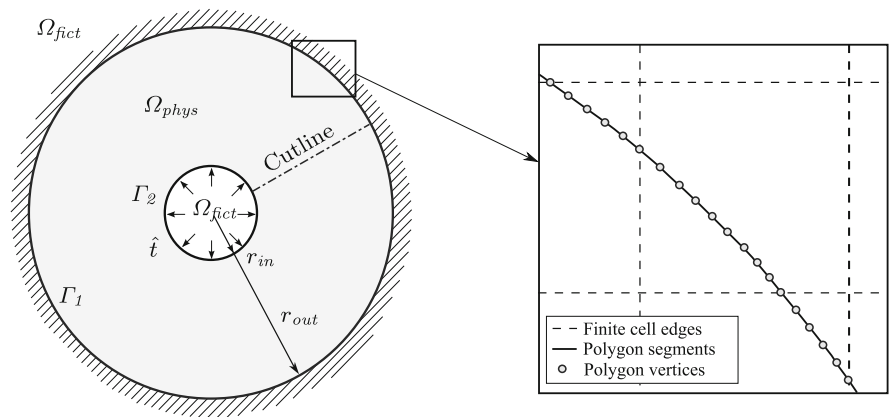

(a)   **(b)**

Fig. 11 Finite cell discretizations with adaptive sub-cells for the ring example. *Open circles* denote element nodes and B-spline knots in the *p*-version and B-spline meshes, respectively, while the *lines in blue* denote integration sub-cells. **a** 4×4 *p*-version cells and sub-cells of depth $m = 5$, **b** 16×16 knot span cells and sub-cells of depth $m = 3$. (Color figure online)

around 0.1% in both the *p*- and B-spline versions, leading to a flattening of the convergence curves. The present example shows that the *p*- and B-spline bases applied in the framework of the Finite Cell concept exhibit an equivalent solution behavior and achieve comparable performance in terms of error level, rates of convergence and flattening of the convergence curve, although their high-order approximation bases are very different.

3.2 Unfitted Dirichlet constraints via Nitsche's method: ring example at small strains

The imposition of unfitted Dirichlet boundary conditions with Nitsche's method is illustrated by the example of a ring in plane strain as shown in Fig. 10. For the present example, curved boundaries are approximated with arbitrary precision by a polygon

$$\boldsymbol{s} : \begin{bmatrix} X^s \\ Y^s \end{bmatrix} = \sum_{i=1}^{n_{vert}} N_i^{lin} (\vartheta) \cdot \begin{bmatrix} X_i^s \\ Y_i^s \end{bmatrix} \tag{22}$$

X_i^s and Y_i^s denote the physical coordinates of the n_{vert} vertices of the polygon in the reference configuration, which lie on Γ. Nodal basis functions $N_i^{lin} (\vartheta)$ defined over parameter space $\vartheta \in [-1, 1]$ linearly interpolate Γ between vertices. Assuming that wherever polygon $\boldsymbol{s}$ crosses a cell edge, a vertex is placed (see Fig. 10), the surface integrals in Eqs. 17 to 18 can be evaluated by placing $p + 1$ Gauss points in the parameter space ϑ of each polygon segment without introducing an additional error from shape function discontinuities at cell edges. This parameterization concept can be analogously applied to three-dimensional problems by introducing a triangular approximation for boundary surfaces of arbitrary geometry [29,33].
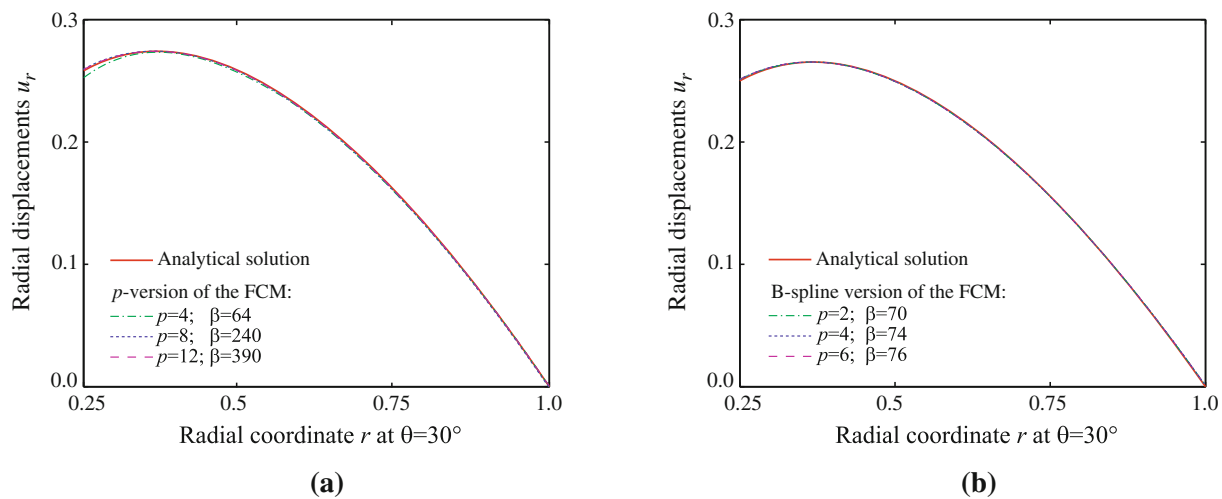
Fig. 12 Radial displacements of the 2D ring example, plotted along the inclined cutline shown in Fig. 10. **a** *p*-version mesh of Fig. 11a, **b** knot span mesh of Fig. 11b

Fig. 13 Von Mises stresses of the 2D ring example, plotted along the inclined cutline shown in Fig. 10. **a** *p*-version mesh of Fig. 11a, **b** knot span mesh of Fig. 11b

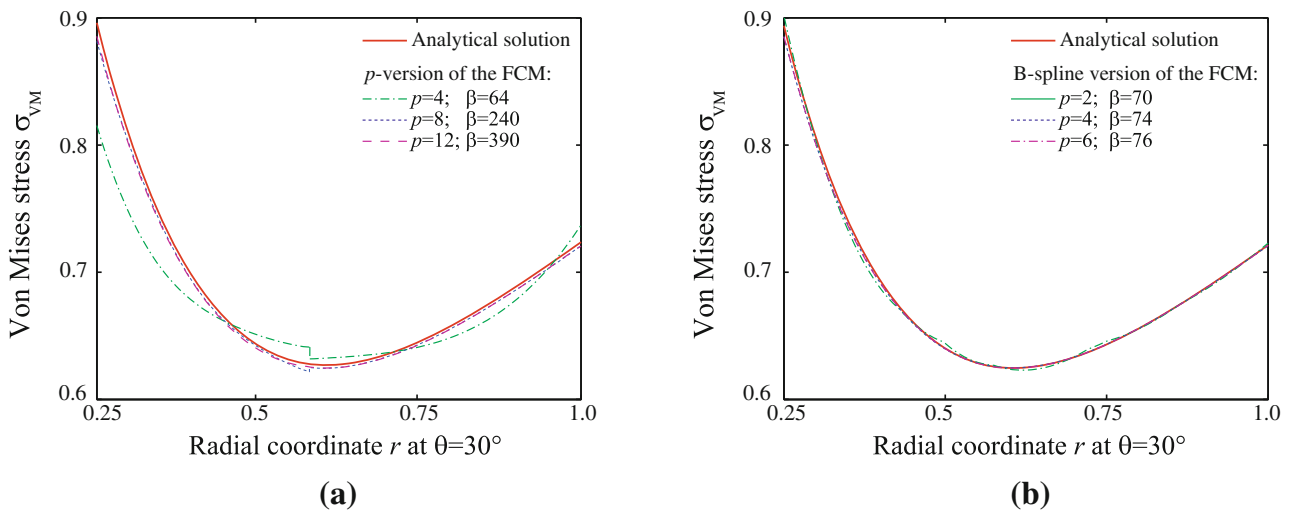The present example specifies radial and circumferential displacements over the Dirichlet boundary Γ_1

$$\hat{u}_r = 0.0; \quad \hat{u}_\theta = 0.0 \tag{23}$$

and radial traction over the Neumann boundary Γ_2

$$\hat{t}_r = \frac{1}{2} \frac{\ln 0.25 + 1}{\ln 2} \tag{24}$$

In addition, radial body forces are applied

$$b_r = \frac{1}{r \ln 2} \tag{25}$$

over the physical domain Ω_{phys}. Assuming the compatible displacement solution in polar coordinates (r, θ) with origin

in the center of the circular ring

$$u_r = -\frac{r}{2} \frac{\ln r}{\ln 2} \tag{26a}$$

$$u_\theta = 0.0 \tag{26b}$$

the corresponding analytical stress fields can be derived by considering basic laws of elastostatics [65]

$$\sigma_r = \varepsilon_r = \frac{\partial u_r}{\partial r} = -\frac{1}{2} \frac{1}{\ln 2} [\ln r + 1] \tag{27a}$$

$$\sigma_\theta = \varepsilon_\theta = \frac{1}{r} \frac{\partial u_\theta}{\partial \theta} + \frac{\partial u_r}{\partial r} = -\frac{1}{2} \frac{\ln r}{\ln 2} \tag{27b}$$

$$\sigma_{r\theta} = 0 \tag{27c}$$

Note that the influence of material parameters does not appear explicitly due to the particular choice of Young's modulus $E = 1.0$ and Poisson's ratio $\nu = 0.0$ (see Fig. 10).
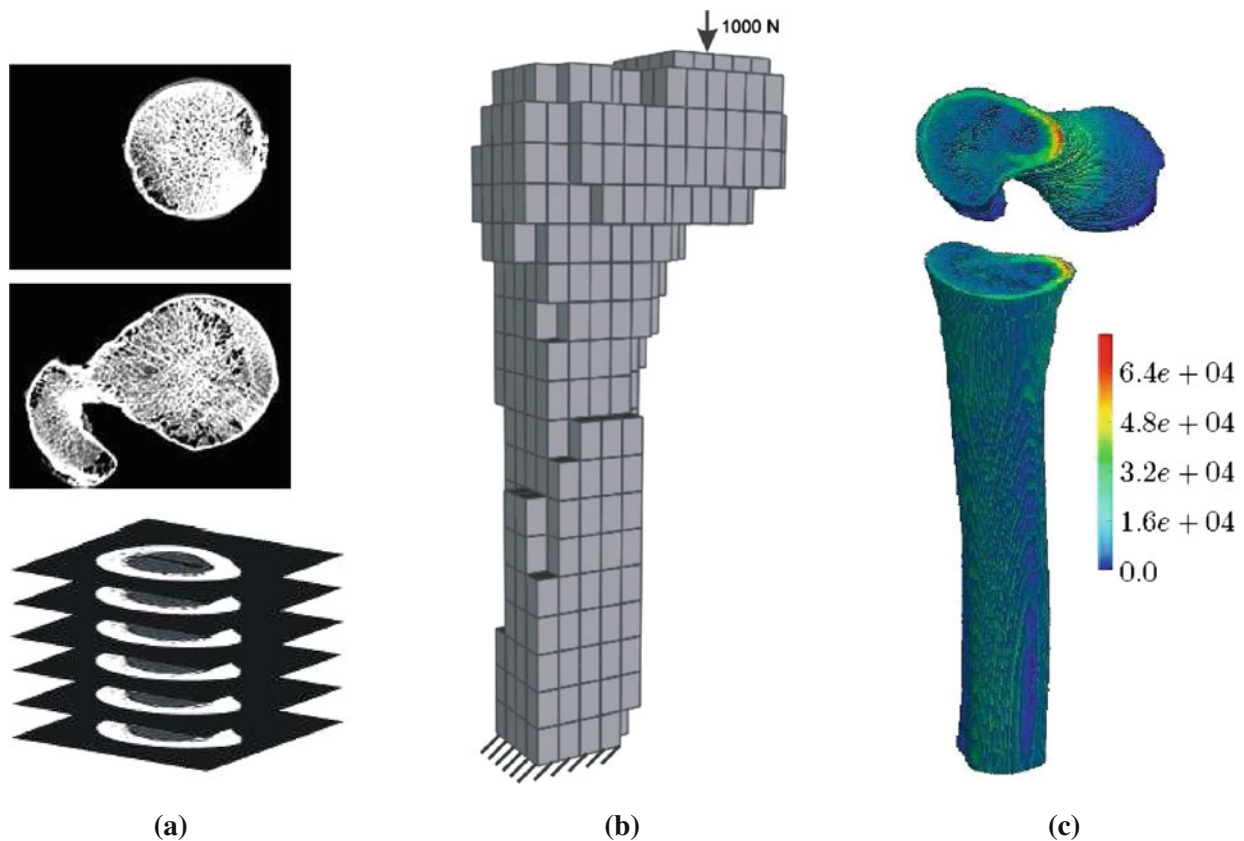
Fig. 14 The Finite Cell Method applied for analysis of a CT-based proximal femur bone. **a** Slices of the CT scan, indicating the thin cortical shell and the trabecular structure inside, **b** Finite Cell mesh of the bone, consisting of 678 p-version finite cells, and boundary conditions, **c** Von Mises equivalent strain distribution [$\mu\varepsilon$], evaluated for each voxel of the physical domain

The discretizations with the p- and B-spline versions of the FCM used in this study consist of 4×4 p-version finite cells and 16×16 knot span cells, which are equipped with $m = 5$ and $m = 3$ levels of adaptive sub-cells as shown in Fig. 11a, b, respectively. Boundary constraints are imposed in a weak sense according to Eqs. 17 and 18. The penalty parameter β is chosen empirically for each discretization and polynomial degree in such a way that β is small, but still keeps the stiffness matrix positive definite. Solutions are obtained from the p-version mesh with polynomial degrees $p = 4$ (322 dofs), $p = 8$ (1,090 dofs) and $p = 12$ (2,370 dofs) and from the B-spline mesh with $p = 2$ (648 dofs), $p = 4$ (800 dofs) and $p = 6$ (968 dofs).

Figures 12 and 13 compare the radial displacement and the von Mises stress results, respectively, to the corresponding analytical reference obtained from Eqs. 26a–26b and 27a–27c. The plots refer to a cutline that originates in the center of the ring and is inclined by an angle of 30° against the horizontal as shown in Fig. 10 to avoid mesh induced symmetry effects. The displacement and stress results converge under p-refinement to the reference and confirm that the weak imposition of Dirichlet boundary conditions via Nitsche's method works well for both the p- and B-spline versions of the FCM. One can observe that for the examined discretizations, the B-spline version achieves a comparable quality in stresses with less degrees of freedom than the p-version due to its higher-order continuity.

3.3 A complex example: analysis of a proximal femur bone with inhomogeneous material

The human femur bone of Fig. 14 is analyzed with the p-and B-spline versions of the FCM on the basis of computed tomography (CT) derived voxel data. This kind of analysis is common in biomechanics to mimic patient-specific in vivo behavior, which allows for a better understanding of bone stability and strength. The majority of research in this field is based on traditional finite elements (see e.g. [66,67]), which are often limited in terms of accuracy and efficiency, the need for time-consuming segmentation of the CT data and an element-wise constant material assignment. Before the discussion of the FCM results, some details on the material model based on voxels are provided.
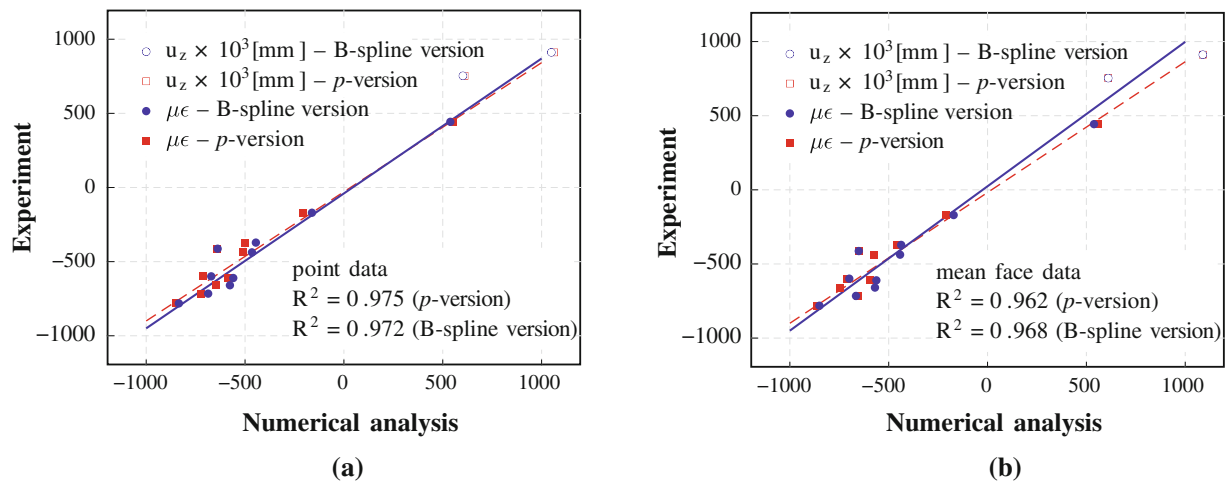
Fig. 15 Experimental results versus simulation results obtained with the *p*- and B-spline versions of the FCM. The target parameter $\mu\varepsilon$ denotes von Mises equivalent strains [33,70,71]. **a** Pointwise values, **b** element face average

3.3.1 A voxel-based model for the representation of inhomogeneous material properties

Voxels are volume elements, aligned in a structured spatial grid in Cartesian directions [68], each of which contains local material information. Voxel data sets have a limited resolution, as precise data is only available at the center of each volume element, and care has to be taken that the chosen voxel resolution represents changes in material parameters accurately enough for simulating the corresponding mechanical behavior. Voxel models of real structures can be directly obtained from computed tomography (CT), magnetic resonance tomography (MRT) or ultrasound scans. For a concise review of medical imaging technologies, see for example [69]. The CT scan of the femur shown in Fig. 14a represents a discrete model[1] of the continuous material distribution with a resolution of $1024 \times 1024 \times 183$ voxels, each providing a measure for the radiodensity of the cortical and trabecular bone regions. First, a radiodensity limit needs to be defined, which separates material from void regions. Since a heterogeneous isotropic material behavior is sufficient to accurately represent the experimental observations [70], the radiodensity scale lying above that limit is translated into a corresponding scale of equivalent material parameters, i.e. Young's modulus E and Poisson's ratio ν, which are then stored independently for each voxel location according to the radiodensity identified there. With the relations given in [66], this results in a different Young's modulus for each voxel and a constant Poisson's ratio of 0.3.

3.3.2 FCM analysis with the p- and B-spline versions

In the *p*-version of the FCM, the bone is embedded in 678 finite cells, each covering $40 \times 40 \times 10$ voxels (see Fig. 14b). Cells that are completely outside the bone are neglected to minimize the computational effort. An equivalent voxel resolution per cell is chosen for the B-spline version of the FCM, but due to the support of the B-spline functions in adjacent cells, none of the cells of the fictitious domain Ω_{fict} can be removed, resulting in a full rectangular grid of 1,729 knot span cells. The inhomogeneity of the material is captured by $20 \times 20 \times 10$ sub-cells per knot span cell, applying 2^3 integration points per sub-cell. Thus the material properties of each voxel within the bone contributes to the analysis model. Integration points outside the physical domain Ω_{phys} are penalized with $\alpha = 10^{-4}$ in the sense of Fig. 1. The proximal femur bone is loaded with 1,000 N on top of the femur head and Nitsche's method according to Eqs. 17 and 18 is applied to weakly satisfy the homogeneous Dirichlet boundary conditions at the distal face (see Fig. 14b) in both FCM versions. Figure 14c illustrates the von Mises equivalent strains obtained from the *p*-version FCM discretization, visualized pointwise for each voxel.

For validation of the numerical results, the linear elasticity response in terms of strains is compared with results from a corresponding in-vitro experiment [33,71]. Figure 15 provides a comparison of the numerical predictions and the experimental results for points located at the strain gauge position of the experiment and averaged results over small surface patches embedding the measuring points. A linear regression analysis shows a good correlation (>0.96) between numerical predictions and measurements for both the *p*- and B-spline versions of the FCM. Sufficient convergence was found for both FCM versions at $p = 4$. For this polynomial

---

[1] Courtesy of Prof. Zohar Yosibash, Dept. of Mechanical Engineering, Ben-Gurion University, Beer-Sheva, Israel; http://www.bgu.ac.il/~zohary/.

degree, the 678 finite cells of the *p*-version result in about 35,000 degrees of freedom, whereas the 1,729 knot span cells of the B-spline version only require about 13,000 degrees of freedom to yield equivalent results at the same accuracy level. The simulation results demonstrate that from an overall point of view, the *p*- and B-spline version of the FCM achieve comparable accuracy in the framework of a very complex example. Readers interested in a detailed description of experiments and FCM analysis are referred to the in-depth study by Ruess et al. [33].

4 A geometrically nonlinear FCM formulation in principal directions

Turning to large deformation analysis, the linear elastic formulation of Sect. 2 is extended in a straightforward manner to a geometrically nonlinear FCM formulation based on logarithmic strains. The adaptation directly follows the standard FE formulation, for which details can be found in [45,72–74].

4.1 Kinematics

In geometrically nonlinear statics, the deformation map $\boldsymbol{\varphi}$ describes the motion of each material particle from its initial reference configuration $\boldsymbol{X}$ to its spatial or deformed configuration $\boldsymbol{x}$.

$$\boldsymbol{x} = \boldsymbol{\varphi}(\boldsymbol{X}) \tag{28}$$

The deformation map Eq. 28 is required to be one-to-one [45,75]. The displacement field $\boldsymbol{u}$ and the deformation gradient $\boldsymbol{F}$ follow as

$$\boldsymbol{u} = \boldsymbol{x} - \boldsymbol{X} \tag{29}$$

$$\boldsymbol{F} = \frac{\partial \boldsymbol{x}}{\partial \boldsymbol{X}} \tag{30}$$

In view of its polar decomposition, $\boldsymbol{F} = \boldsymbol{V}\boldsymbol{R}$ can be represented by the rotation tensor $\boldsymbol{R}$ and the spatial stretch tensor $\boldsymbol{V}$. Therefore, $\boldsymbol{V}^2$ can be obtained from the left Cauchy-Green tensor

$$\boldsymbol{b} = \boldsymbol{F}\boldsymbol{F}^T = (\boldsymbol{V}\boldsymbol{R})\left(\boldsymbol{R}^T\boldsymbol{V}\right) = \boldsymbol{V}^2 \tag{31}$$

Evaluation of the principal directions of $\boldsymbol{V}^2$ yields the orthogonal spatial Eigenvector triad $\{\boldsymbol{n}_1, \boldsymbol{n}_2, \boldsymbol{n}_3\}$ and the associated Eigenvalues $\{\lambda_1^2, \lambda_2^2, \lambda_3^2\}$, which are identified as the squared principal stretches. The spatial logarithmic strain tensor $\boldsymbol{\varepsilon} = \ln \boldsymbol{V}$ in spectral form reads

$$\boldsymbol{\varepsilon} = \sum_{a=1}^{3} \ln \lambda_a \, \boldsymbol{n}_a \otimes \boldsymbol{n}_a \tag{32}$$

Logarithmic strains, also known as true or natural strains, represent a suitable strain measure for the entire deformation
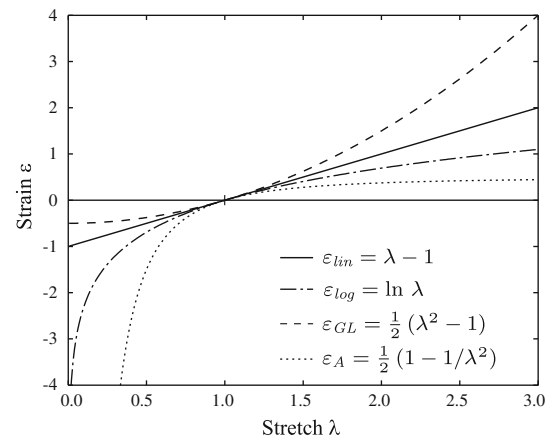

Fig. 16 Engineering, logarithmic, Green-Lagrange and Almansi strain measures $\varepsilon_{lin}, \varepsilon_{log}, \varepsilon_{GL}, \varepsilon_A$, respectively, in one dimension

range [45,73], and are compared in 1D to other common nonlinear strain measures in Fig. 16.

In the framework of the Finite Cell concept as described in Sect. 2, the nonlinear kinematic relations Eqs. 28 to 32 can be applied throughout the complete embedding domain Ω (see Fig. 1). This approach is referred to as the standard geometrically nonlinear FCM formulation in the following. Due to the discontinuous penalization parameter α of Eq. 3, the analytical deformation map and corresponding displacements Eqs. 28 and 29 exhibit a weak discontinuity (kink) along the geometric boundaries of the physical domain Ω_{phys}. Accordingly, the analytical deformation gradient and related stretches and strains Eqs. 30 to 32 exhibit a strong discontinuity (jump).

4.2 Constitutive equations in principal directions

The Hencky hyperelastic model is the finite logarithmic strain based extension of the standard linear elastic material, whose strain energy function Ψ reads [45,73]

$$\Psi = \alpha \cdot \left[\frac{E}{2(1+\nu)} \left((\ln \lambda_1)^2 + (\ln \lambda_2)^2 + (\ln \lambda_3)^2 \right) \right.$$
$$\left. + \frac{\nu E}{2(1+\nu)(1-2\nu)} (\ln J)^2 \right] \tag{33}$$

with $J = \det \boldsymbol{F} = \lambda_1 \lambda_2 \lambda_3$ and material parameters Young's modulus E and Poisson's ratio ν. In the standard FCM formulation, geometric nonlinearity is applied throughout the complete domain Ω. Therefore, Eq. 33 is factorized by parameter α of Eq. 3, which penalizes the strain energy function Ψ within the fictitious domain Ω_{fict}. The principal
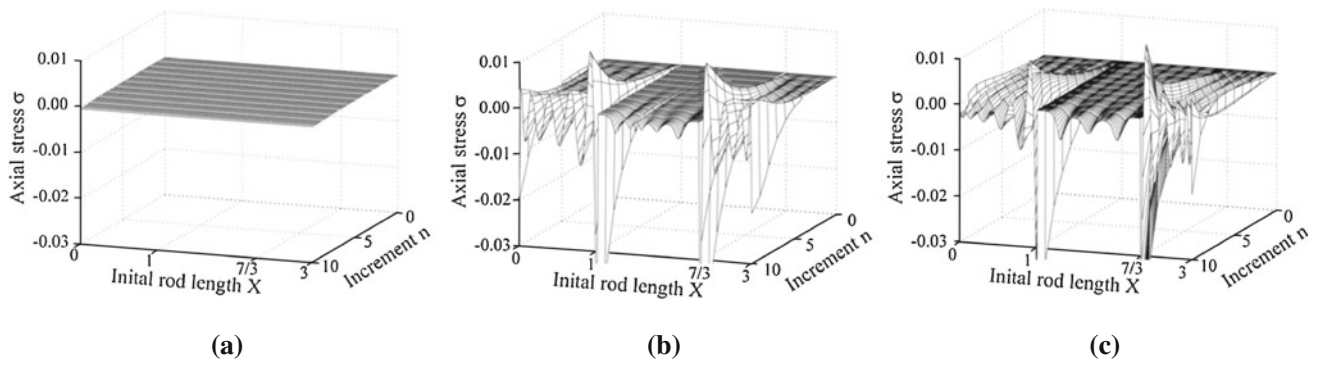
Fig. 17 Stresses of the geometrically nonlinear rod example, obtained with the standard FCM formulation and $p = 15$, are compared to the analytical solution with a finite value $\alpha = 10^{-5}$. **a** Analytical, **b** p-version, **c** B-spline version

Cauchy stresses along principal axes $a = \{1, 2, 3\}$ follow with Eq. 33 as

$$\sigma_a = \frac{1}{J} \frac{\partial \Psi}{\partial \ln \lambda_a}$$
$$= \frac{\alpha}{J} \left[\frac{E}{(1 + \nu)} \ln \lambda_a + \frac{\nu E}{(1 + \nu)(1 - 2\nu)} \ln J \right] \quad (34)$$

The fourth order spatial elasticity tensor in Cartesian coordinates can then be computed as

$$c_{ijkl} = \sum_{a,b=1}^{3} \frac{1}{J} \frac{\partial^2 \Psi}{\partial \ln \lambda_a \partial \ln \lambda_b} \eta_{aabb} - \sum_{a=1}^{3} 2\sigma_a \eta_{aaaa}$$
$$+ \sum_{\alpha,\beta=1}^{3} \frac{\sigma_a \lambda_b^2 - \sigma_b \lambda_a^2}{\lambda_a^2 - \lambda_b^2} \left(\eta_{abab} + \eta_{abba} \right) \quad (35)$$

implying the fourth order dyadic product $\eta_{ijkl} = n_i \otimes n_j \otimes n_k \otimes n_l$. Due to the strong discontinuity in α, all derived analytical quantities exhibit a loss of regularity along geometric boundaries.

4.3 Discretization, linearization and the Newton–Raphson procedure

Taking into account Eqs. 28 to 35, the variational formulation of standard FCM for large deformation elasticity can be derived from the principle of virtual work

$$\delta W (\varphi, \delta u) = \int_{\varphi(\Omega)} \sigma : \nabla_x \delta u dv - \int_{\varphi(\Omega_{phys})} b \cdot \delta u dv$$
$$- \int_{\varphi(\Gamma_N)} t \cdot \delta u da = 0 \quad (36)$$

with body forces b, traction vector t and test function δu. Integrals are evaluated in the deformed configuration, where dv and da denote infinitesimal volume and area elements, respectively, since a spatial formulation is computationally more efficient in the case of p-version elements [76–78].

The basic kinematic quantities u, δu and F can be discretized in the sense of Eqs. 4, 5 and by

$$F = I + \sum_{a=1}^{n} \nabla_X N_a u_a \quad (37)$$

where N_a denote shape functions of a suitable high-order basis. In case of finite cells based on p-version basis functions, insertion of the displacement approximation Eq. 4 and the reference configuration, interpolated subparametrically by Eq. 11, into Eq. 29 yields an interpolation of the deformed configuration

$$x = \sum_{i=1}^{n_{vert}} N_i^{nod} X_i + \sum_{a=1}^{n} N_a u_a \quad (38)$$

For finite cells based on high-order B-splines, the corresponding expression can be found with Eq. 16 as

$$x = X_0 + h \, \xi + \sum_{a=1}^{n} N_a u_a \quad (39)$$

where h is the uniform width of the knot span cells and X_0 the physical origin in the parameter space ξ.

Using these expressions in Eq. 36, the discretized virtual work per high-order mode shape a can be formulated as the difference between the internal and external equivalent force vectors f^{int} and f^{ext}, called residual r

$$\delta W (\varphi, N_a \delta u_a) = \delta u_a^T \left(f_a^{int} - f_a^{ext} \right) = \delta u_a^T r_a \quad (40)$$

$$f_a^{int} = \int_{\varphi(\Omega)} B_a^T \sigma dv \quad (41)$$

$$f_a^{ext} = \int_{\varphi(\Omega_{phys})} N_a b dv + \int_{\varphi(\Gamma_N)} N_a t da \quad (42)$$

with the strain–displacement matrix B [1,2,45]. The linearization of the discretized weak form Eq. 36 in the direction of an incremental displacement Δu can be expressed in terms
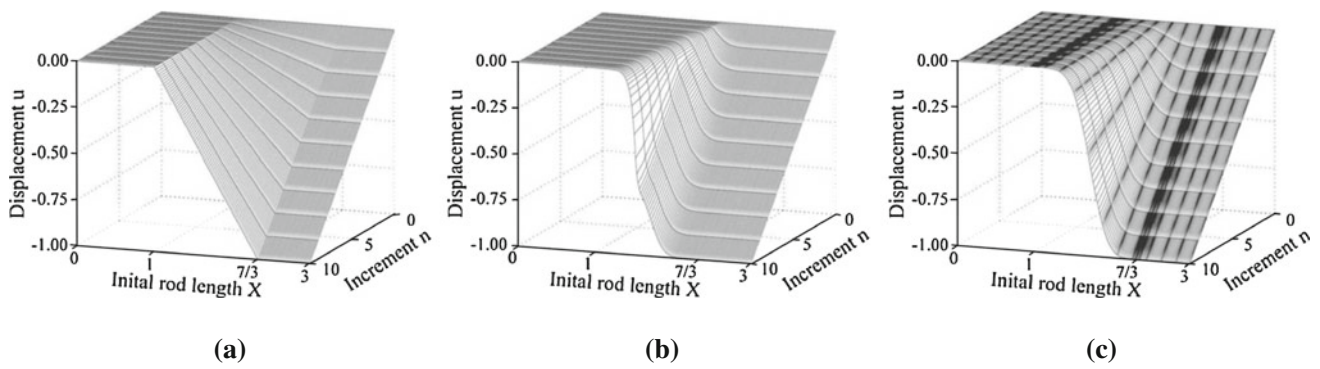
Fig. 18 Displacements of the geometrically nonlinear rod example, obtained with the modified FCM formulation and $p = 15$. The reference solution was computed with three conforming standard linear elements. **a** Reference, **b** p-version, **c** B-spline version
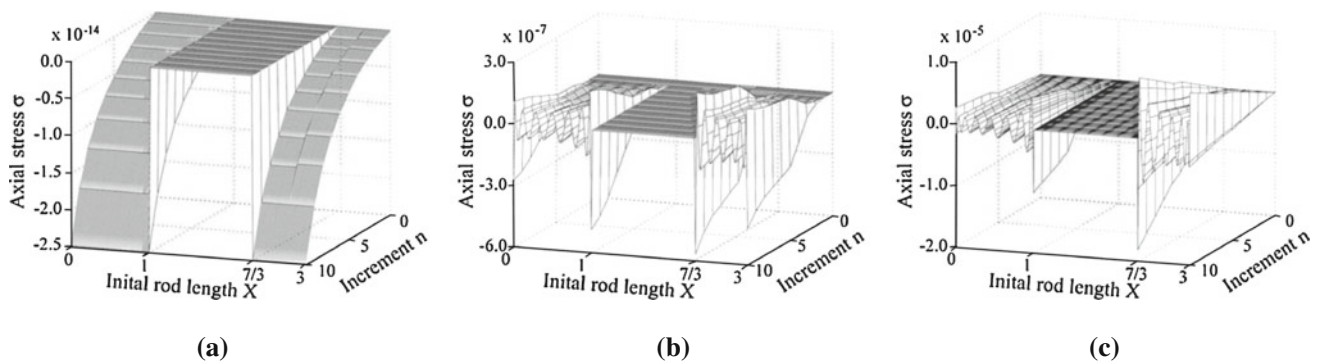

Fig. 19 Stresses of the geometrically nonlinear rod example, obtained with the modified FCM formulation and $p = 15$. The reference solution was computed with three conforming standard linear elements. **a** Reference, **b** p-version, **c** B-spline version

of material and geometric parts $D\delta W_c$ and $D\delta W_\sigma$, respectively, as

$$D\delta W \left(\boldsymbol{\varphi}, N_a \delta \boldsymbol{u}_a\right) \left[N_b \Delta \boldsymbol{u}_b\right] = D\delta W_c + D\delta W_\sigma \tag{43}$$

$$D\delta W_c = \delta \boldsymbol{u}_a^T \left(\int\limits_{\varphi(\Omega)} \boldsymbol{B}_a^T \boldsymbol{c} \, \boldsymbol{B}_b dv \right) \Delta \boldsymbol{u}_b \tag{44}$$

$$D\delta W_\sigma = \delta \boldsymbol{u}_a^T \left(\int\limits_{\varphi(\Omega)} \left(\nabla_X N_a \cdot \boldsymbol{\sigma} \, \nabla_X N_b\right) \boldsymbol{I} dv \right) \Delta \boldsymbol{u}_b \tag{45}$$

with $\boldsymbol{c}$ being the matrix representation of the spatial elasticity tensor Eq. 35 [45]. In Eqs. 44 and 45, the expressions in brackets can be identified as the entries $K_{c,ab}$ and $K_{\sigma,ab}$ of the material and geometric tangent stiffness matrices, respectively. Combining Eqs. 36 and 40 yields

$$\left(\boldsymbol{K}_c + \boldsymbol{K}_\sigma\right) \Delta \boldsymbol{u} = -\boldsymbol{r} \tag{46}$$

from which the classical Newton–Raphson procedure can be derived. In each Newton step, the linearized system Eq. 46 is solved for $\Delta \boldsymbol{u}$, which updates the total displacements $\boldsymbol{u}$,

until the norm of the residual vector $\boldsymbol{r}$ has converged below a tolerance close to zero. In the scope of the present article, the stiffness contribution due to deformation dependent loads [45,74] is not discussed. For a treatment within the framework of the p-version and B-spline version of the FCM, see [34] and [52], respectively.

5 Deformation resetting: a modified geometrically nonlinear FCM formulation

The geometrically nonlinear formulation for the one-dimensional rod of Fig. 7 simplifies to

$$\Psi = \alpha \frac{E}{2} \left(\ln \lambda\right)^2 \tag{47}$$

$$\sigma = \alpha \frac{E}{J} \ln \lambda \tag{48}$$

$$c = \alpha \frac{E}{J} - 2\sigma \tag{49}$$

with axial stretch λ and the determinant of the deformation gradient $J = \lambda^{1-2v}$ [45]. To illustrate the influence of large deformations within the fictitious domain, the sine load $f_{\sin}$ of Fig. 7 is neglected for a moment and the prescribed displacement is set to a large value of $\Delta u = 1.0$. Nonetheless, the physical stresses should be zero, since a rigid body movement of the right part of the rod is approximated. Thus, the resulting non-zero stresses directly reflect the modeling error due to the finite value of α and the numerical error. In all computations of the present section, the total displacement load is divided into 10 increments, each of which needs 2 to 4 Newton–Raphson iterations to converge to a L^2-norm of the residual below 10^{-12}, and Dirichlet boundary conditions are imposed strongly. The exact stress solution, which can be derived analytically according to [51], is plotted in Fig. 17a for 10 displacement load increments between 0 and Δu and $\alpha = 10^{-5}$.

5.1 The standard FCM formulation with geometric nonlinearity in Ω_{phys} and Ω_{fict}

First, the behavior of the 1D rod example is examined, if the same geometrically nonlinear formulation is applied over the complete embedding domain Ω as described in Sect. 4. The only difference between Ω_{phys} and Ω_{fict} in this case constitutes the penalization of the strain energy function Ψ Eq. 33 and its derivatives with α of Eq. 3. However, numerical experiments with the 1D example reveal that the smallest penalty parameter, which could be used successfully for each tested polynomial degree p, is $\alpha = 10^{-4}$ and $\alpha = 10^{-5}$ for the p- and B-spline version, respectively. Corresponding solution fields obtained with 2 p-version finite cells and 16 knot span cells in the sense of Fig. 7 are plotted in Fig. 17b, c. For α smaller than these bounds, the determinant of the deformation gradient F falls below zero at some integration point within Ω_{fict}, which inevitably terminates the computation. From a mathematical point of view, this implies the loss of uniqueness of the deformation map, which is not one-to-one anymore. From a physical point of view, this can be interpreted as a penetration of material, which constitutes a severe violation of the principles of continuum mechanics [45,74,75]. With α as large as 10^{-4}, the penalization of Eq. 3 is unable to sufficiently eliminate the influence of Ω_{fict}, so that a considerable modeling error is introduced. In addition, the strain energy contribution of Ω_{fict} is amplified by the nonlinear strain measure. Whereas engineering strains of linear elasticity are bound by definition to very small values $|\varepsilon_{lin}| \ll 1.0$, logarithmic strains of nonlinear elasticity are able to grow without bounds in order to yield physically meaningful measures for very large deformation states. However, in case of large deformations in the fictitious domain, nonlinear strains thus act as an additional counterbalance to α and increasingly outweigh the penalization.

As a consequence, the contribution of Ω_{fict} to the total strain energy Eq. 19 grows, so that the nonlinear FCM scheme tries to accurately fit the solution in both the fictitious and physical domains due to the best approximation property discussed in Sect. 3.1. Thus, solution fields do not extend smoothly into the fictitious domain, but develop large oscillations throughout the discontinuous cells (see Fig. 17). The corresponding convergence deteriorates to a low algebraic rate, which is a well-known issue for high-order elements with inter-element discontinuities [30]. Numerical experiments indicate that standard FCM formulations based on other nonlinear strain measures (see [45,73] and Fig. 16) in combination with corresponding constitutive equations affect the stability of the deformation map in the same way. The standard FCM formulation of Sect. 4 thus suffers from a conflict of interest between stable analysis (increase of α) on the one hand and a reduction of the contribution of Ω_{fict} (decrease of α) on the other.

5.2 A modified formulation based on repeated deformation resetting in Ω_{fict}

To avoid the stability problem of the deformation map in the fictitious domain Ω_{fict}, the physical consistency of the geometrically nonlinear FCM formulation is restricted to the physical domain Ω_{phys}. Within Ω_{fict}, the formulation is manipulated in such a way that stable geometrically nonlinear analysis with very small values $\alpha < 10^{-10}$ is possible. Numerical experiments reveal that problems with the uniqueness of the deformation map occur at the location of maximum deformation within the fictitious domain Ω_{fict}. This motivates the following simple manipulation after each Newton iteration i

$$\varphi^i(\mathbf{X}) = \begin{cases} \mathbf{x}^i & \text{deformed configuration} \quad \forall X \in \Omega_{phys} \\ \mathbf{X} & \text{reset to reference} \\ & \text{configuration} \quad \forall X \in \Omega_{fict} \end{cases} \tag{50}$$

where φ^i and $\mathbf{x}^i$ denote the deformation map and the deformed configuration after the ith Newton step. According to Eq. 50, the deformation is repeatedly reset to the initial undeformed state to erase the complete deformation history within Ω_{fict}. Thus, at the beginning of the $(i + 1)$th Newton iteration, the deformation gradient Eq. 30 in Ω_{fict} is defined as

$$\mathbf{F} = \mathbf{I} \tag{51}$$

with $\mathbf{I}$ being the unit tensor. From Eq. 51, the corresponding principal stretches Eq. 32 and stresses Eq. 34 directly follow as

$$\lambda_a = 1.0, \quad a = \{1, 2, 3\} \tag{52}$$

$$\boldsymbol{\sigma} = \mathbf{0} \tag{53}$$

The resulting formulation is inconsistent, because it violates the principles of continuum mechanics and its analytical solution in Ω_{fict} turns unphysical. However, in the sense of the fictitious domain approach (see Fig. 1), it does not affect the physical consistency and accuracy of the solution in the physical domain Ω_{phys}, provided that the influence of Ω_{fict} and its contribution to the total strain energy Eq. 19 are extenuated by a sufficiently strong penalization.

The assumption of Eq. 51 supersedes the calculation of the deformation gradient, so that any stability issues resulting from the numerical computation of the deformation gradient are automatically avoided and a very small penalty parameter of $\alpha = 10^{-15}$ can be applied without any further problems. The corresponding stress and displacement fields obtained with the p- and B-spline versions are plotted in Figs. 18 and 19, respectively. The repeated resetting of the deformation allows for a smooth extension of FCM solution fields into the fictitious domain despite the presence of discontinuities in the corresponding analytical solutions (see Figs. 18, 19). The oscillatory behavior demonstrated in Fig. 17 for the stress solutions obtained with the standard FCM formulation is still present, but is considerably reduced by several orders of magnitude.

For a computationally efficient implementation of the deformation resetting, the coincidence of linear and geometrically nonlinear elasticity at the deformation and stress free reference configuration can be exploited [45,72–74]. Since the deformation resetting switches Ω_{fict} back to its reference configuration after each Newton iteration, it is fully equivalent to carrying out repeated linear elastic computations

$$\delta W = \begin{cases} \delta W\,(\boldsymbol{\varphi}, \delta\boldsymbol{u}) & \text{large deformation} \quad \forall \boldsymbol{X} \in \Omega_{phys} \\ \delta W\,(\boldsymbol{u}, \delta\boldsymbol{u}) & \text{small displacements} \quad \forall \boldsymbol{X} \in \Omega_{fict} \end{cases} \quad (54)$$

Numerical experiments show that provided a sufficiently small penalty parameter, the quadratic rate of convergence of the Newton algorithm can be fully maintained.

5.3 Convergence in strain energy

To test convergence in energy measure in terms of Eqs. 20 and 21 [79], the uni-axial rod of Fig. 7 is considered with sine load $f_{\sin}$ and $\Delta u = 1.0$. An overkill discretization with 1,000 cubic finite elements taking into account the left rod yields $U_{ex} = 1.17182588 \times 10^{-5}$. The convergence for p-refinement in the p- and B-spline versions with a standard geometrically nonlinear formulation is plotted in Fig. 20. It illustrates the convergence decay to a low algebraic rate of around $q = 1.0$ on average, which can be attributed to the modeling error introduced by insufficient penalization in conjunction with oscillatory stresses (see Fig. 17). The modified geometrically nonlinear formulation allows for a con-
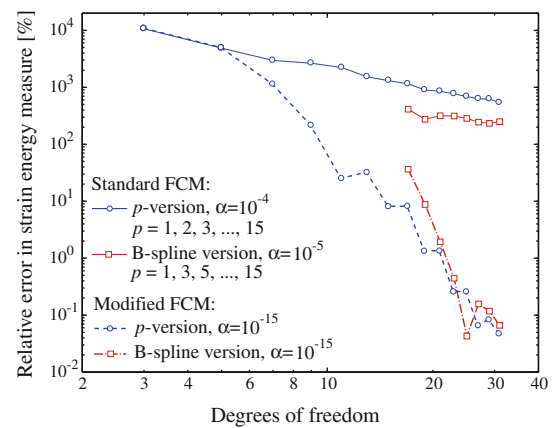

Fig. 20 Convergence of the nonlinear 1D example

siderable decrease of the penalty parameter to $\alpha = 10^{-15}$, which reduces the modeling error and the oscillatory behavior in stresses considerably (see Fig. 19). Using the modified formulation, both p- and B-spline versions of the FCM are able to achieve exponential convergence with maximum rates of $q = 18.13$ and $q = 28.09$, respectively (see Fig. 20). The flattening of the convergence curves indicate a take-over of the influence from Ω_{fict} at a value of around 0.04%. Under the assumption that the rate of the standard FCM formulation could be continued, approximately 30,000 times as many degrees of freedom (around 1 million) would be required to achieve a comparable level of accuracy.
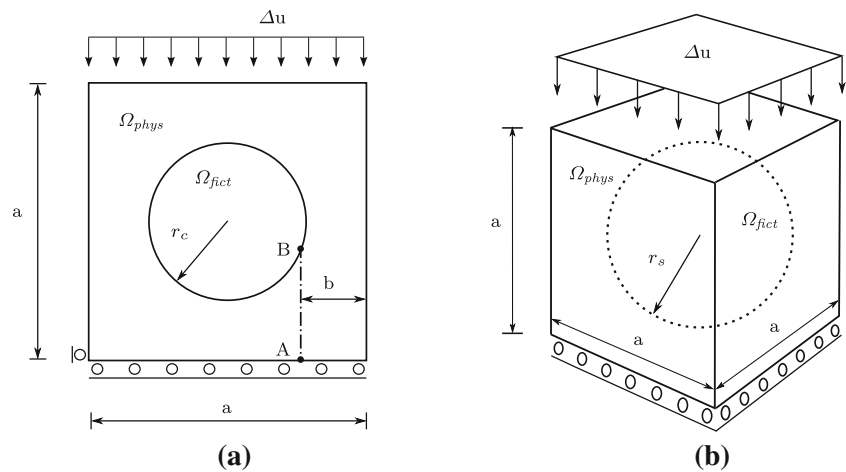
6 A geometrically nonlinear penalty method for the weak imposition of Dirichlet constraints

In the 1D example shown so far, Dirichlet boundary conditions could be imposed strongly by standard FE techniques. More complex examples in two- and three dimensions require their imposition along boundaries cutting through cells, which can be achieved in a weak sense with the help of Nitsche's method as presented in Sects. 2 and 3 for linear elastic problems.

6.1 Penalty versus Nitsche's method

The penalty method [56–58] is a subset of Nitsche's method and can be obtained from Eqs. 17 and 18 by omitting the so-called consistency terms that involve the computation of the normal vector $\boldsymbol{n}$ [59,63]. It is based on the remaining terms that involve the penalty parameter β and has similar advantages as Nitsche's method, e.g. it creates no additional unknowns and preserves the banded structure, symmetry and positive definiteness of the stiffness matrix. However, in contrast to Nitsche's method, it is not consistent in a variational sense [59,63] and can lead to strongly ill-conditioned system matrices. At least the latter does not affect the

Fig. 21 Benchmark examples: parameters are width/height a; plate thickness t; radius r; Young's modulus E; domains Ω_{phys} and Ω_{fict}; Poisson's ratio ν; prescribed displacements Δu; cut line AB. **a** 2D plate with circular hole, parameters: $a = 2.0$; $b = 0.45$; $t = 0.1$; $\Delta_u = 0.3$, $r_c = 0.75$, $\Omega_{phys} : E = 1.0$; $\Omega_{fict} : \alpha E$; $\nu = 0.2$. **b** 3D cube with spherical hole, parameters: $a = 2.0$; $\Delta_u = 0.3$; $r_s = 0.6$; $\Omega_{phys} : E = 1.0$; $\Omega_{fict} : \alpha E$; $\nu = 0.2$

FCM in the present form, since system matrices are already ill-conditioned due to the penalization of the fictitious domain with α of Eq. 3.

In the framework of geometrically nonlinear problems, Nitsche's method requires the consistent linearization of all additional terms in Eqs. 17 and 18. Due to the missing consistency terms, the linearization of the penalty method is considerably simplified. Therefore, the penalty method is applied in the following for the weak imposition of Dirichlet boundary conditions.

6.2 Discretization and linearization

The penalty method in variational form [57,58] is based on the addition of a penalty term δW_p to the geometrically nonlinear variational equation of the principle of virtual work Eq. 36 [1,2]. The penalty term, obtained by integration over the Dirichlet boundary Γ_D (see Fig. 1), can be formulated in the reference configuration as

$$\delta W_p (\boldsymbol{u}, \delta\boldsymbol{u}) = \beta \int_{\Gamma_D} (\boldsymbol{u} - \hat{\boldsymbol{u}}) \cdot \delta\boldsymbol{u} dA \tag{55}$$

where $\boldsymbol{u}$, $\hat{\boldsymbol{u}}$ and $\delta\boldsymbol{u}$ denote vectors of unknown displacements, prescribed displacements on Γ_D and test functions, and β is a scalar penalty parameter. The consistent derivation of the penalty method is based on a constrained minimization problem, formulated with the help of Lagrange multipliers, for which Eq. 55 constitutes an approximation (see for example [1,2] for an overview and [80] for details). Note that inhomogeneous Dirichlet boundary conditions, which constrain displacements in one special direction, can be easily implemented by applying the penalty parameter β only to the vector components of the constrained direction.

Using Eqs. 4 and 5 in Eq. 55, the discretized virtual work of the penalty term δW_p at a known displacement state $\boldsymbol{u}$ results in the internal and external equivalent force vectors $\boldsymbol{f}_p^{int}$ and $\boldsymbol{f}_p^{ext}$, respectively, which can be expressed per high-order mode shape a as

$$\boldsymbol{f}_{a,p}^{int} = \beta \int_{\Gamma_D} \boldsymbol{u} \, N_a dA \tag{56}$$

$$\boldsymbol{f}_{a,p}^{ext} = \beta \int_{\Gamma_D} \hat{\boldsymbol{u}} \, N_a dA \tag{57}$$

The linearization of the discretized virtual work of the penalty term Eq. 55 in the direction of an incremental displacement $\Delta\boldsymbol{u}$ can be found by taking the Gâteaux derivative [45,75], which simply yields

$$D\delta W_p = \delta\boldsymbol{u}_a^T \left(\beta \int_{\Gamma_D} N_a N_b dA \right) \Delta\boldsymbol{u}_b \tag{58}$$

The expression in brackets can be identified as the entries $K_{p,ab}$ of the penalty contribution to the tangent stiffness matrix. Equation 58 is independent of the current state of deformation $\boldsymbol{u}$ and remains therefore constant throughout all iterations. Note that all quantities resulting from the penalty term are evaluated in the reference configuration [45,75], since a push-forward to the deformed configuration leads to a more involved expression due to the vector format of the area mapping (Nanson's formula) [75].

Combining the penalty tangent stiffness $\boldsymbol{K}_p$ with material and geometric tangent stiffnesses $\boldsymbol{K}_c$ and $\boldsymbol{K}_\sigma$, respectively, and adding the equivalent internal and external forces Eqs. 56 and 57 to the right hand side results in the following discrete system of equations

$$\left(\boldsymbol{K}_c + \boldsymbol{K}_\sigma + \boldsymbol{K}_p \right) \Delta\boldsymbol{u} = -\boldsymbol{r} \tag{59}$$

$$\boldsymbol{r} = \left(\boldsymbol{f}^{int} + \boldsymbol{f}_p^{int} \right) - \left(\boldsymbol{f}^{ext} + \boldsymbol{f}_p^{ext} \right) \tag{60}$$

from which the classical Newton–Raphson procedure can be derived in the sense of Eq. 46.
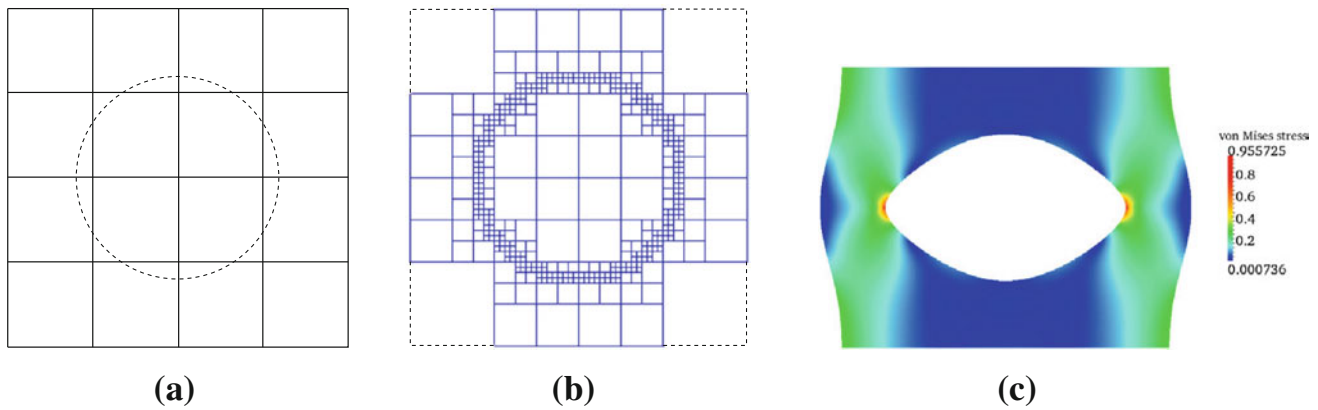
Fig. 22 2D plate with circular hole, computed with the p-version of the FCM. **a** FCM mesh consisting of 4×4 p-version cells, **b** integration sub-cells displayed up to level $k = 4$, **c** Von Mises stresses on the deformed configuration, obtained with $p = 15$
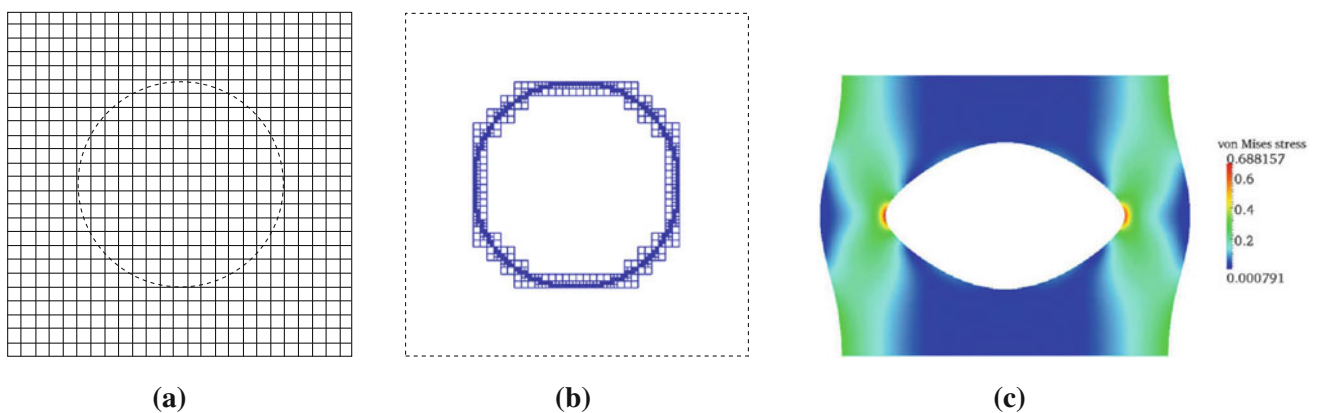

Fig. 23 2D plate with circular hole, computed with the B-spline version of the FCM. **a** FCM mesh consisting of 25×25 p-version cells, **b** integration sub-cells displayed up to level $k = 3$, **c** Von Mises stresses on the deformed configuration, obtained with $p = 15$

7 Numerical examples at large strains (1): benchmarks in 2D and 3D

Accuracy and computational efficiency of the modified geometrically nonlinear FCM formulation are further examined for three benchmark problems. Our implementation of both FCM versions is based on Sandia's library framework Trilinos [81] and uses the direct solver Pardiso [82]. Its results are compared to overkill solutions derived with standard linear quadrilateral and quadratic tetrahedral elements on conforming meshes, provided by the open-source nonlinear finite element code FlagShyp [83]. Conforming mesh generation is accomplished by the meshers Visual Domesh [84] and Netgen [85], visualization is done with ParaView [86].

7.1 Plate with a circular hole

The first example problem consists of a 2D square plate in plane stress, which is perforated by a circular hole. Material and geometric parameters as well as boundary conditions are given in Fig. 21a. For the FCM computations, the origin of

the coordinate system is placed in the center of the circular hole. Thus, its geometry can be implicitly represented by the inequality $X^2 + Y^2 \leq r_c^2$, which allows for an efficient point location query at each Gauss point to determine the corresponding penalty parameter α of Eq. 3. The complete domain Ω is discretized by a structured FCM mesh of $4 \times 4 p$-version finite cells and 25×25 knot span cells shown in Figs. 22a and 23a, respectively, and complemented by integration sub-cells displayed in Figs. 22b and 23b. The adaptive structure of the sub-cells, each of which is equipped with $(p + 1) \times (p + 1)$ Gauss points, leads to an aggregation of integration points around geometric boundaries, so that the discontinuity in α can be accurately resolved. To minimize the integration error, a sub-cell quadtree with overly large depths $m = 8$ and $m = 4$ is applied throughout all computations with the p- and B-spline version, respectively. Dirichlet constraints can be imposed strongly, since Dirichlet boundaries conform to cell boundaries. The displacement load is divided in three equally sized increments, each of which requires not more than 3–4 Newton iterations in both FCM versions to converge to a value of the L^2-norm of the
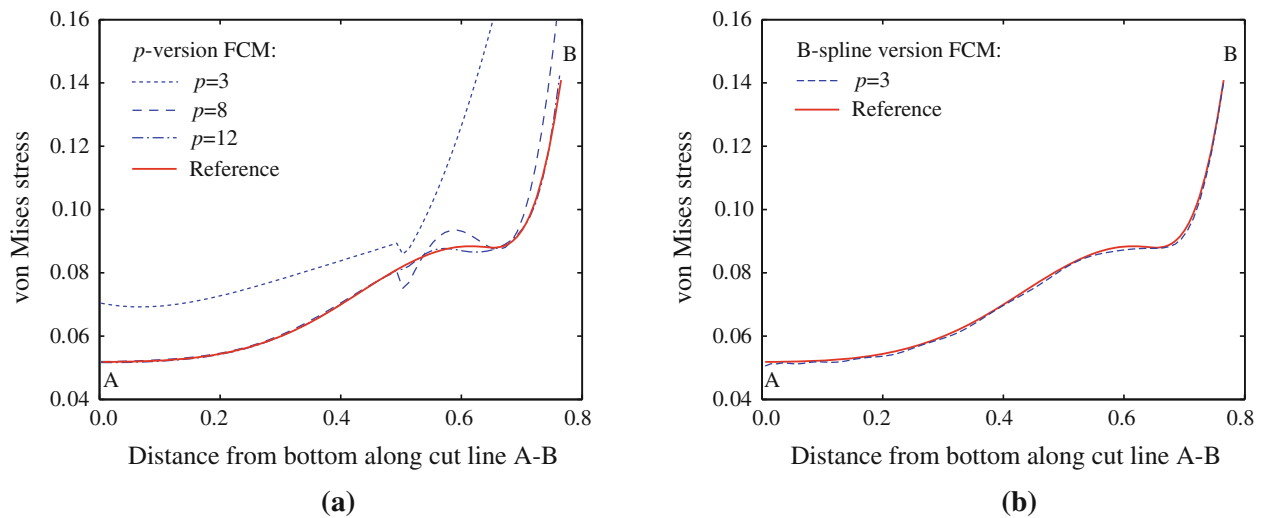
Fig. 24 Von Mises stresses along cut line A–B of the 2D plate with circular hole, obtained with the *p*-version and B-spline discretizations shown in Figs. 22 and 23, respectively. *p*-version (**a**) and B-spline version (**b**) of the FCM

residual below 10^{-12}. The modified FCM formulation allows for a penalization of Ω_{fict} with $\alpha = 10^{-15}$.

A first impression of the quality of the geometrically non-linear FCM solutions can be obtained from the von Mises stress plots shown in Figs. 22c and 23c obtained with polynomial degree $p = 15$. Both FCM versions are able to accurately localize the typical stress concentration at the vertical edges of the circular hole and are free of stress oscillations in the physical domain. For the computation of a reference solution in terms of strain energy, the symmetry in geometry and boundary conditions is made use of to reduce the plate to 1/4 of the original system. The considered FlagShyp discretization with a mesh conforming to the geometric boundaries consists of 224,312 standard linear quadrilateral elements and 449,723 degrees of freedom, taking into account the physical domain Ω_{phys} only. Figure 24a, b give a more detailed view of the quality of the stress solution by plotting von Mises stresses along cut line A–B (see Fig. 21a), obtained from the *p*- and B-spline discretization, respectively, and the FlagShyp reference solution. Both FCM versions converge to the reference, while stresses are accurate and smooth up to the geometric boundary at point B. Comparing the *p*-version solution of $p = 12$ (2,270 dofs) and the B-spline solution of $p = 3$ (1,299 dofs), one can observe that the high-order continuity of B-splines achieves a more accurate stress solution at a lower polynomial degree with less degrees of freedom, while the reduced C^0-continuity along the *p*-version cell boundary leads to jumps.

Multiplying the strain energy, which has been obtained by the FlagShyp discretization of the quarter system, by four yields a reference $U_{ex} = 2.305691 \times 10^{-3}$ for the complete system. Convergence studies with different mesh sizes indicate that the given U_{ex} is correct up to the sixth decimal,

so that relative errors in terms of Eq. 20 being larger than 0.1% can be reliably determined. For the finite cell meshes of the *p*- and B-spline versions given in Figs. 22a and 23a, respectively, a *p*-refinement study is performed. Using the overkill result from the Flagshyp discretization as a reference, Fig. 25a reveals that both FCM versions are able to achieve exponential rates of convergence in strain energy. At an error level of 0.1%, the convergence curves level off due to the impact of the finite value of the penalty parameter α. The jumps in the convergence curve of the B-spline version can be attributed to the influence of the integration error.

The reason for the different mesh sizes in the *p*- and B-spline versions lies in the different behaviour of the support of the corresponding basis functions under *p*-refinement. To illustrate that statement, let us consider the 4×4 *p*-version mesh of Fig. 22a. According to Sect. 2.3, the support of the nodal, edge and internal modes under *p*-refinement is invariant, being a maximum of 4×4, 2×2 and 1×1 finite cells, respectively. However, for B-spline basis functions, the maximum support spans $(p+1) \times (p+1)$ finite cells (see Sect. 2.4) and thus rapidly increases with the polynomial degree p considered. A corresponding 4×4 knot span mesh exhibits one basis function with global support at $p = 3$, nine at $p = 5$, and almost all of its basis functions are global at $p = 15$. On the one hand, such a discretization will lead to an almost fully populated stiffness matrix with full bandwidth. The B-spline version in this form can thus be characterized a spectral method rather than a finite element scheme. At the same time, it is considerably less accurate than a *p*-version mesh, since it contains much less degrees of freedom. At $p = 15$ for example, 4×4 knot span cells exhibit approx. 750 dofs, while approx. 3,500 dofs are created in a 4×4 *p*-version mesh. Therefore, a comparison of *p*-version and
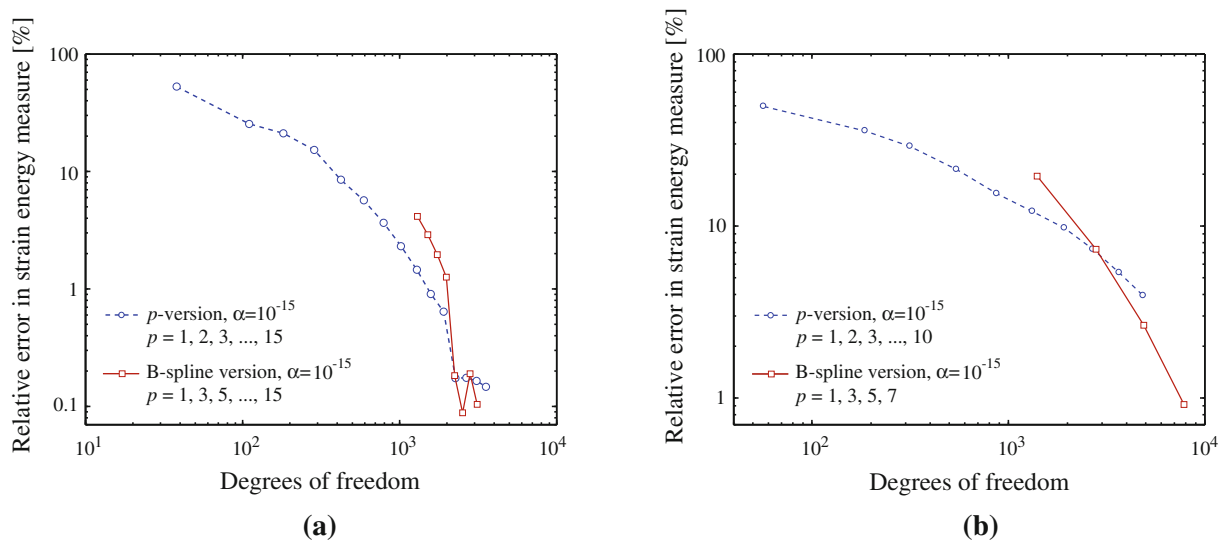
Fig. 25 Convergence behavior of the 2D and 3D benchmark examples obtained with the modified FCM formulation. **a** 2D plate with circular hole, **b** 3D cube with spherical hole

B-spline discretizations with the same number of cells seems not appropriate to us and is not presented in the scope of this study. Instead, the number of knot span cells is increased in such a way that p-version and B-spline meshes exhibit approximately the same amount of degrees of freedom and the maximum support of a single B-spline basis function is smaller than the complete domain Ω under consideration.

7.2 Cube with a spherical hole

The 3D analogue of the perforated square plate is a cube with a spherical hole, whose geometry, material and boundary conditions are given in Fig. 21b. The geometry of the sphere is again described implicitly by the inequality $X^2 + Y^2 + Z^2 \leq r_s^2$, which allows for efficient point location queries in 3D. The complete domain Ω is discretized by a structured FCM mesh of $2 \times 2 \times 2$ p-version cells and $7 \times 7 \times 7$ knot span cells as shown in Figs. 26a and 27a, respectively. The finite cell meshes are complemented by adaptive sub-cells to take into account the discontinuity in α during numerical integration. In Figs. 26b and 27b, only one half of the symmetric sub-cell structures are displayed to uncover their adaptive resolution of the spherical boundary. Dirichlet constraints can again be imposed strongly, since Dirichlet boundaries coincide with cell faces. For the solution of the geometrically nonlinear system, the displacement load is divided in three equally sized increments, each of which requires in both FCM versions only 3–4 Newton iterations to converge to a value of the L^2-norm of the residual below 10^{-10}. The modified FCM formulation allows for a penalization with $\alpha = 10^{-15}$.

A first impression of the quality of the geometrically nonlinear FCM solutions can be obtained from the von Mises stress plots given in Figs. 26c and 27c obtained with polynomial degree $p = 7$. To allow an insight into the 3D stress state, only 1/8 of the symmetric system is displayed. Both FCM versions are able to accurately localize the stress concentration around the spherical boundary. Moreover, the physical domain Ω_{phys} does not exhibit stress oscillations. For the computation of a strain energy reference, the symmetry in geometry and boundary conditions is again made use of to reduce the cube to 1/8 of the original system. The considered FlagShyp discretization with a mesh conforming to the geometric boundaries consists of 15,300 standard 10-node quadratic tetrahedrals with 69,862 degrees of freedom. Multiplying the resulting strain energy by 8 yields $U_{ex} = 6.6008376 \times 10^{-2}$. Convergence studies with different mesh sizes indicate a accuracy up to the fourth decimal, so that relative errors being larger than 1.0% can be reliably determined. Performing a p-refinement study on the given finite cell discretizations, one can determine the convergence behavior in strain energy with respect to the given reference. The results shown in Fig. 25b confirm also for the 3D case that exponential rates of convergence can be achieved with both the p-version and the B-spline version of the FCM.

7.3 Unfitted Dirichlet constraints via the penalty method: ring example at large strains

The performance of the penalty method for the imposition of unfitted Dirichlet boundary conditions in the framework of the geometrically nonlinear FCM is examined by the ring
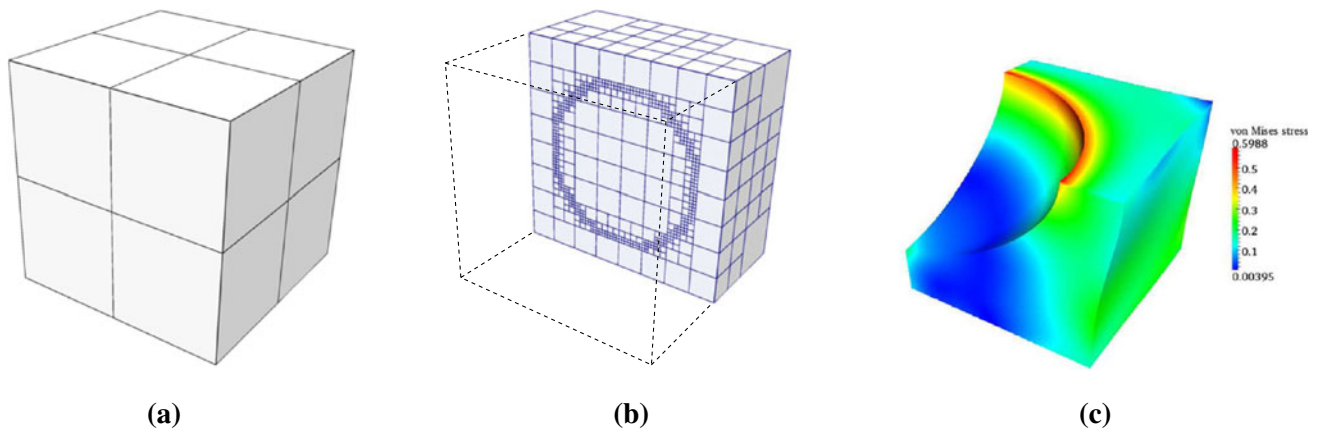
Fig. 26 3D cube with spherical hole, computed with the *p*-version of the FCM. Note that only one half of the symmetric sub-cell structure is displayed to uncover their adaptive resolution of the spherical bound- ary of the hole. **a** FCM mesh consisting of $2 \times 2 \times 2$ *p*-version cells, **b** adaptive integration sub-cells of level $m = 5$, **c** Von Mises stresses on the deformed configuration ($p = 7$)
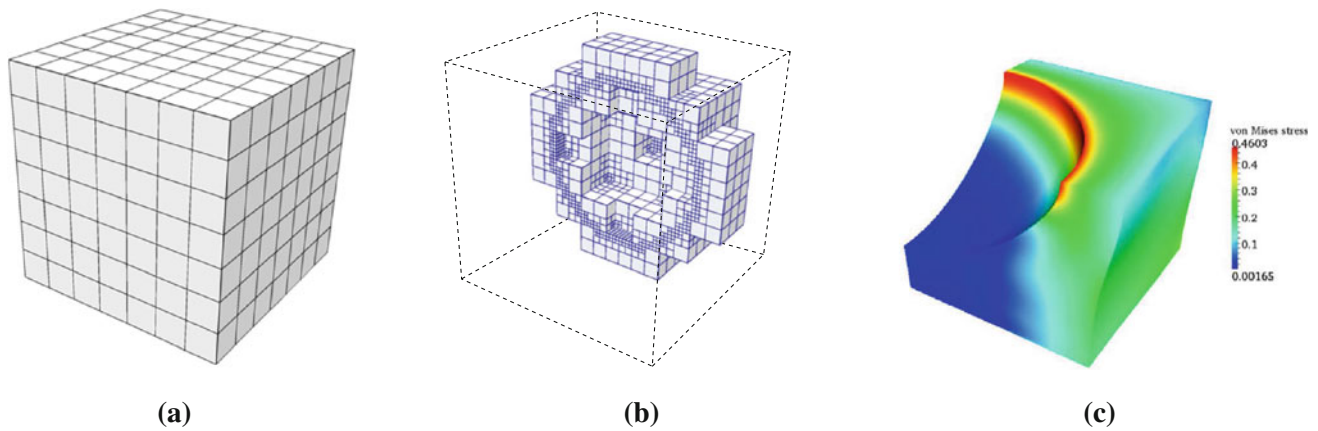

Fig. 27 3D cube with spherical hole, computed with the B-spline ver- sion of the FCM. Note that only one half of the symmetric sub-cell structure is displayed to uncover their adaptive resolution of the spher- ical boundary of the hole. **a** FCM mesh consisting of $7 \times 7 \times 7$ knot span cells, **b** adaptive integration sub-cells of level $m = 3$, **c** Von Mises stresses on the deformed configuration ($p = 7$)

example of Fig. 10. The problem set is maintained with the only exceptions that geometrically nonlinear kinematics are assumed, body forces are omitted and traction over the inner boundary Γ_2 is replaced by a non-zero displacement bound- ary condition

$$\hat{u}_r = 0.25; \quad \hat{u}_\theta = 0.0 \tag{61}$$

The ring is discretized with the *p*- and B-spline versions of the FCM as shown in Fig. 11a, b, where the inner and outer cir- cles are approximated in the sense of Eq. 22 by an overly large number of 20,212 and 38,612 polygon segments in order to minimize the corresponding error influence. For the solution of the geometrically nonlinear system, the displacements on Γ_2 are divided into three equally sized increments, each of which requires 4–5 Newton–Raphson iterations to converge to a norm of the residual below 10^{-12}. Figure 28a, b shows the regular and symmetric mesh deformation in the physi- cal domain for the *p*-version and B-spline discretizations,

respectively, which confirms that the physical domain is not influenced by the presence or the modified FCM formula- tion of the surrounding fictitious domain. Figure 29a, b plot the corresponding total displacement solutions on the initial configuration, which show the expected circular pattern. The maximum values are located at the inner Dirichlet bound- ary and are accurate with respect to Eq. 61 up to the fourth decimal in both FCM versions.

For the computation of the corresponding relative errors in strain energy Eq. 20, U_{ex} is computed by an overkill dis- cretization in FlagShyp, which applies 41,400 linear quadri- laterals conforming to geometric boundaries for one quarter of the symmetric ring. Multiplying the resulting total strain energy by four yields a reference for the complete system of $U_{ex} = 0.2855052$. Figure 30 shows the convergence in strain energy measure, obtained by *p*-refinement of the *p*-version and B-spline discretizations. For each polynomial degree *p*, parameter β is empirically chosen in both FCM
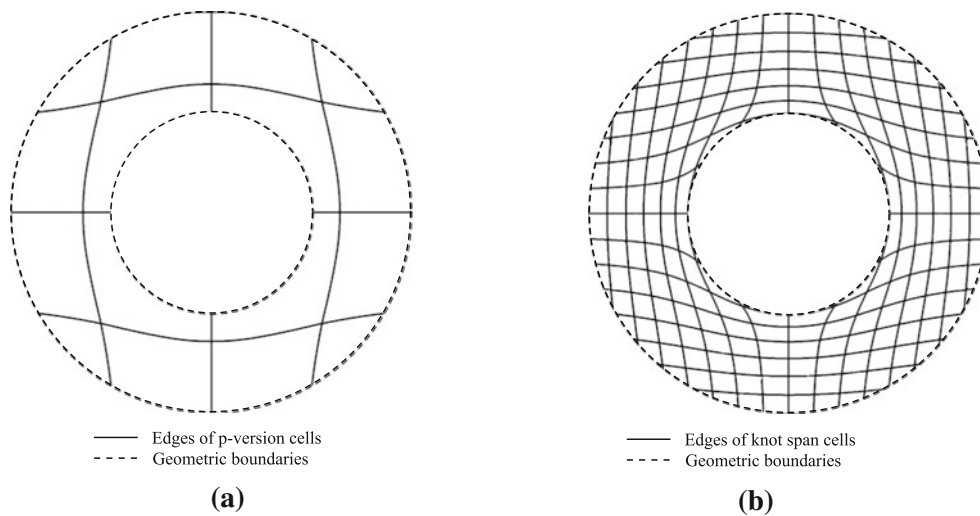
Fig. 28 Deformed finite cell meshes of Fig. 11, plotted over the physical domain, for the ring example at large strains. **a** 4×4 p-version cells, **b** 16×16 knot span cells
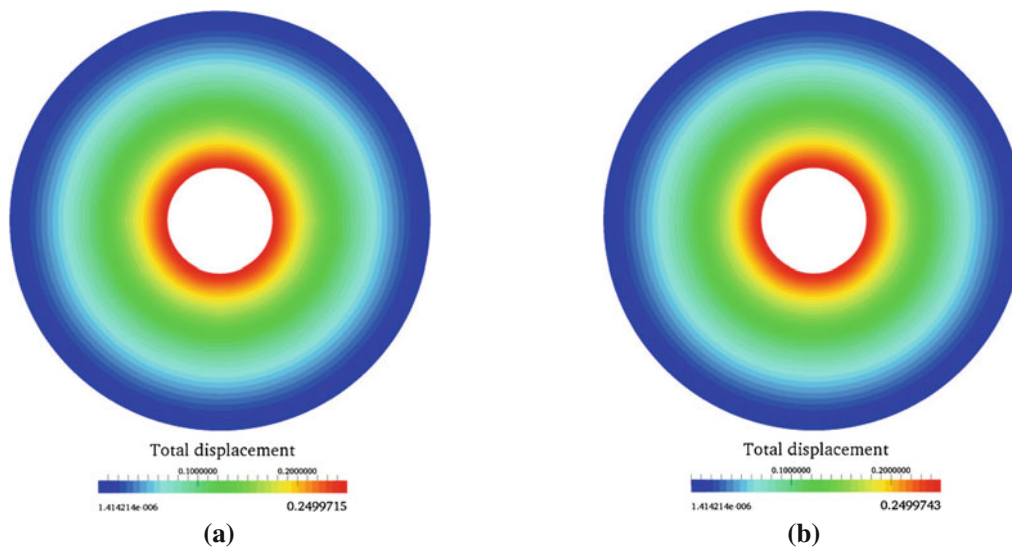

Fig. 29 Total displacements plotted on the initial configuration, obtained with the above meshes at $p = 7$. **a** p-version, **b** B-spline version

version within the interval $\left[10^5, 10^7\right]$, so that the corresponding solution yields a minimum error in strain energy. It can be observed that exponential rates of convergence can be achieved for the p- and B-spline versions. However, the convergence curve flattens at an error level of around 1%, due to the influence of the finite penalization parameters α and β. A detailed examination and discussion of possible effects of the penalty parameter β on the condition number of the stiffness matrix and the convergence of the p-version of the FCM are provided in [38]. The present example confirms the potential of the penalty method for incorporating unfitted Dirichlet boundary conditions, while maintaining the key advantages of FCM in terms of simple mesh generation and exponential rates of convergence.

8 Numerical examples at large strains (2): robustness under severe mesh distortion

Previous studies on large deformation analysis with p-version [77,87] and isogeometric finite elements [4,88,89] show that higher-order and higher-continuity shape functions permit increased levels of mesh distortion. In large deformation FCM, severe distortion of the structured FCM mesh may occur as a result of the mapping of cells from the reference to the deformed configuration. In the scope of the present paper, the ability of the p- and B-spline versions of the FCM to use the robustness of their high-order bases for the representation of very large deformation states is illustrated by the geometrically nonlinear benchmark of a beam under torsion,
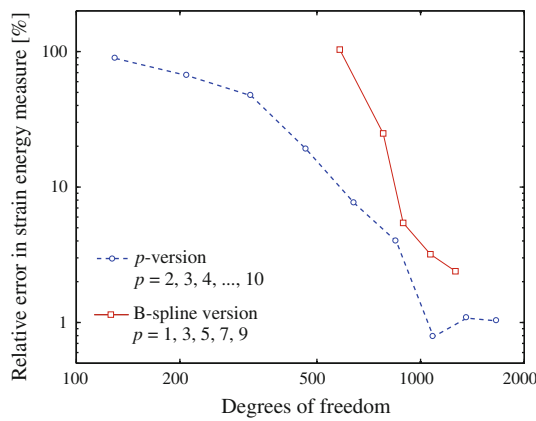
Fig. 30 Convergence of the relative error in strain energy measure for the ring example at large strains
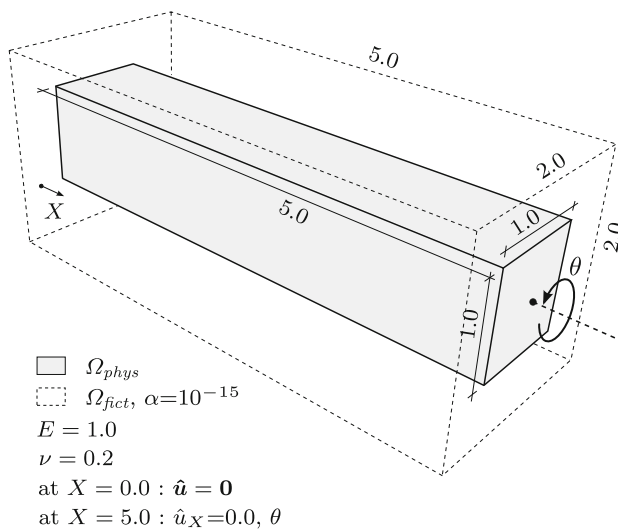

Fig. 31 Beam under torsion

for which a system sketch and material properties are given in Fig. 31. The dimensions of the beam are chosen according to Lipton et al. [89], where the example is examined for incompressible large deformation elasticity. Torsion is imposed by a Dirichlet boundary constraint, rotating the cross-sectional plane at one end of the beam by angle θ, while the cross-section at the opposite end of the beam is completely fixed.

For testing the solution behavior of the FCM, the beam is embedded in a fictitious domain Ω_{fict} of dimensions $5 \times 2 \times 2$, which contains the physical domain Ω_{phys} in its center as illustrated in Fig. 31 and is penalized by parameter $\alpha = 10^{-15}$ in the sense of Fig. 1. The modified geometrically nonlinear formulation introduced in Sect. 5 is applied. Corresponding discretizations with the p- and B-spline versions of the FCM, consisting of $8 \times 3 \times 3$ p-version cells of $p = 3$ with 2,508 degrees of freedom and $11 \times 5 \times 5$ knot span cells of $p = 3$ with 2,688 degrees of freedom, are displayed in Fig. 32a, b, respectively, and are comparable in terms of

polynomial degree and number of degrees of freedom. Due to the cuboidal geometry of the beam, integration of the FCM stiffness matrix contributions can be accomplished exactly with $m = 2$ levels of integration sub-cells, which conform to the discontinuity in α. Unfitted Dirichlet boundary conditions at both ends are imposed weakly via the penalty method with $\beta = 10^6$, leaving all boundary parts of Ω_{fict} unconstrained.

First, the behavior of the finite cell versions for moderately large deformations is examined by imposing a rotation angle of $\theta = 180°$ (half a rotation around the beam axis). To obtain a qualitative reference, a regular finite element analysis with the p-version of the FEM is performed. The conforming FE mesh consists of $20 \times 4 \times 4$ high-order elements of polynomial degree $p = 6$ with 43,110 degrees of freedom. In analogy to the FCM, Dirichlet constraints are enforced via the geometrically nonlinear penalty formulation presented in Sect. 6. The resulting von Mises stress and the corresponding deformation pattern are shown in Fig. 33. Corresponding solutions obtained with the p- and B-spline version of the FCM are displayed in Figs. 34 and 35, respectively. The deformed FCM meshes illustrating the behavior of the parts of the finite cells in the physical domain show a regular deformation pattern, in particular the cells cut by the geometric boundary. The corresponding von Mises stresses match well with the reference of Fig. 33 despite the presence of the fictitious domain. One can identify a slight advantage of the B-spline version, which comes closer in terms of the maximum and minimum stress values and provides a C^2-continuous stress pattern, while the p-version exhibits jumps across the C^0-continuous cell boundaries. The displacement and stress results show no observable effect from the distortion of the FCM meshes on the displacement and stress accuracy.

Second, the behavior of the finite cell versions under extreme deformations is examined by imposing a rotation angle of $\theta = 1,080°$ (three complete rotations around the beam axis). Corresponding solutions obtained with the p- and B-spline versions of the FCM are displayed in Figs. 36 and 37, respectively. Deformed FCM meshes in the physical domain, in particular the finite cells cut by the geometric boundary, still show a regular deformation pattern with the expected helix-like shape despite a considerable distortion of the cells. The corresponding von Mises stresses show a qualitative agreement at first sight, but a closer look reveals that there are some differences in terms of maximum and minimum values and the location of stress peaks. Due to its higher-order continuity, the B-spline results lead again to smoother deformation and stress patterns than the p-version results. To find the limit deformation states for the present example, representable with the p-version and B-spline discretizations of Fig. 32a, b, the rotation angle θ is continuously increased in increments of $\Delta\theta = 9°$, until the nonlinear mapping in the physical domain fails due to numerical problems.
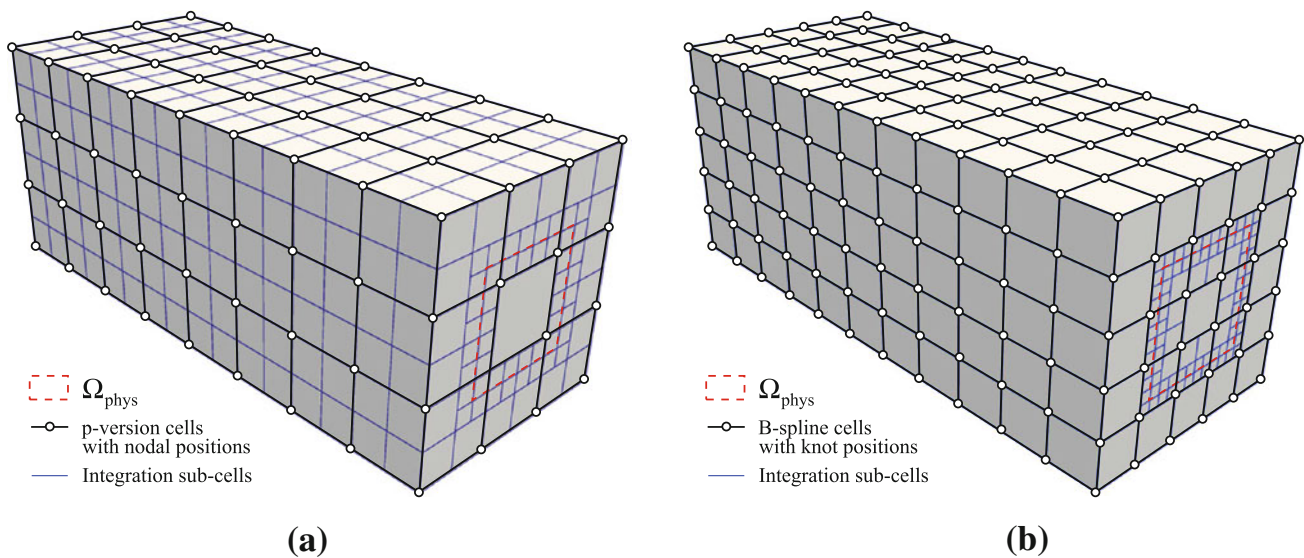
(a)

(b)

Fig. 32 Discretization of the complete domain with the *p*- and B-spline versions of the FCM. **a** 72 cubic *p*-version finite cells with 2,508 degrees of freedom, **b** 265 cubic knot span finite cells with 2,688 degrees of freedom

The *p*-version of the FCM is able to represent a maximum rotation of the beam of $\theta = 1,107°$, whereas the knot span finite cell mesh of the B-spline version achieves a slightly larger maximum of $\theta = 1,143°$.

Figures 38 and 39 illustrate the distortion of the fictitious domain for moderately and extremely large deformations by plotting the corresponding deformed meshes in Ω_{fict}. From the point of view of the typical FCM solution behavior discussed in Sect. 3.1, it is beneficial for the quality of the FCM results, if the solution fields in the fictitious domain can "move" as freely as possible to permit a smooth extension of the physical solution into the fictitious domain. For the moderately large rotation of the beam, this freedom is provided to a comparable extent by both FCM versions (see Fig. 38). For the very large rotation of the beam, the deformation in the fictitious domain of the *p*-version discretization is considerably larger than the corresponding deformation in the B-spline discretization. Note that Fig. 39a, b exhibit dif-

ferent scales, and can be related to each other only by comparison with the deformed physical mesh. The difference in deformation indicates that in the presence of extremely large deformations, the C^0-continuous *p*-version can better accomplish a smooth extension of the solution fields than the B-spline version, where the higher-order continuity of the basis functions seems to constrain larger deformations in the fictitious domain. Due to the modified formulation with deformation resetting in Ω_{fict}, the extreme distortion of the mesh in the fictitious domain does not affect the overall numerical stability of the FCM scheme, since the corresponding geometrically linear computations always assume the reference configuration and a nonlinear mapping does not need to be computed. The resulting deformation in the fictitious domain completely lacks physical meaning and an arbitrary penetration of the deformed meshes may occur.

The results of the beam under extremely large rotation clearly indicate that the FCM fully inherits the robustness of the high-order bases. Both FCM versions are able to represent extremely large deformation states despite severe distortion of the physical part of the corresponding mesh. However, the influence of the fictitious domain on the solution fields of the physical part might be increased, in particular in higher-continuity B-spline discretizations.
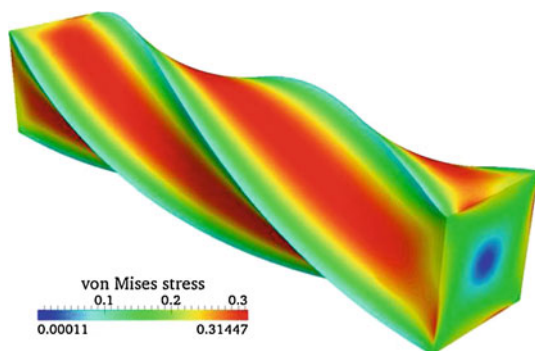

von Mises stress

Fig. 33 Qualitative reference for the beam rotated by $\theta = 180°$, obtained with standard high-order FEM

9 Numerical examples at large strains (3): analysis of complex voxel-based geometries

The fundamental advantage of the FCM is the very simple and fast grid generation irrespective of the geometric com-
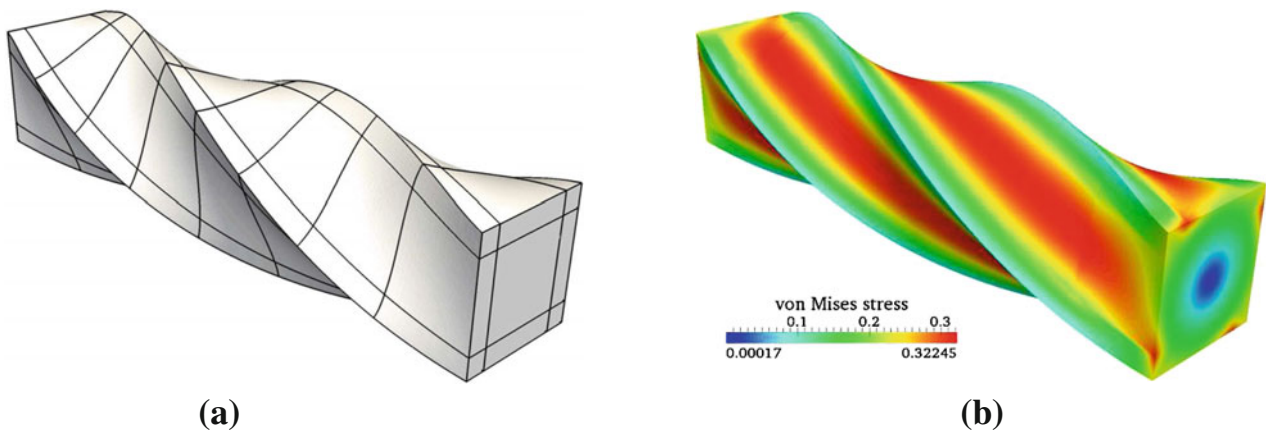
Fig. 34 The beam under a moderately large rotation of $\theta = 180°$ computed with the B-spline version of the FCM. **a** Deformed p-version cell mesh in the physical domain. The fictitious domain part is cut away, **b** Von Mises stress plotted on the deformed configuration
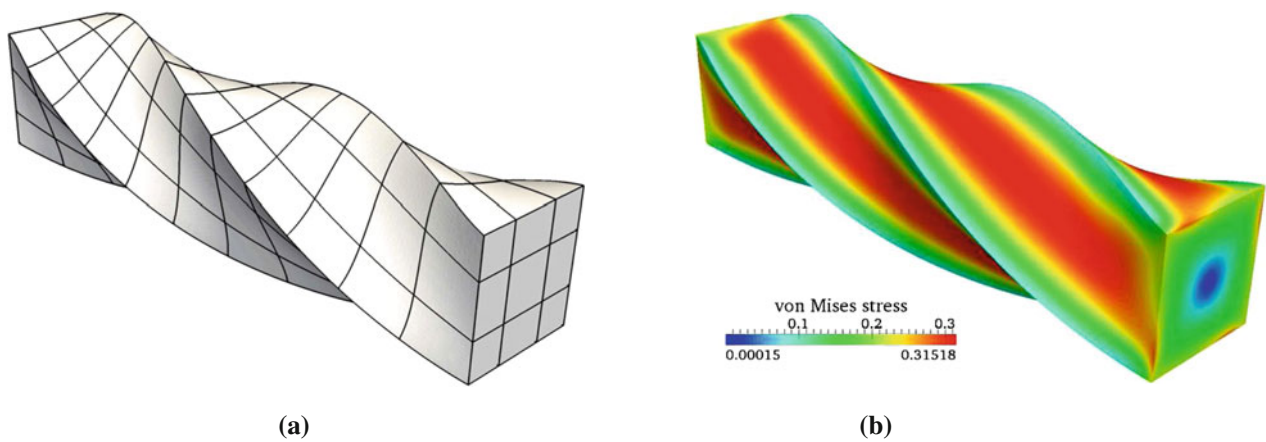

Fig. 35 The beam under a moderately large rotation of $\theta = 180°$, computed with the B-spline version of the FCM. **a** Deformed knot span cell mesh in the physical domain. The fictitious domain part is cut away, **b** Von Mises stress plotted on the deformed configuration

plexity involved. It is based on the disconnection of the high-order grid from the geometry, which is instead represented by the change of parameter α at integration point level. In the following, the straightforward integration of complex voxel-based geometries in FCM analysis is demonstrated by the geometrically nonlinear simulation of a metal foam.

9.1 Efficient generation of adaptive integration sub-cells from voxel models

The standard way of representing very complex three-dimensional geometries are volumetric models based on voxel partitioning [68]. The example of a voxel-based geometrical model of a bone structure, accommodating inhomogeneous material properties, has been presented in Sect. 3.3. If the structure consists of a single material, the voxel information required for FCM analysis consists solely of the penalty parameter α. The information necessary at each voxel location can then be reduced to a bit code $b_{vox} \in \{0, 1\}$,

which determines whether there is material ($b_{vox} = 1$) or a void ($b_{vox} = 0$). Thus, geometric boundaries of the physical domain Ω_{fict} are represented by the change of b_{vox} from one voxel to the next. The bit encoding significantly speeds up input/output operations and minimizes memory requirements with respect to a direct storage of the floating point number α. The bit code can be simply generated from a CT scan by defining a radiodensity limit, below which b_{vox} is set to zero, while everything above is set to one. The CT-based open cell aluminium foam sample[2] shown in Fig. 40 illustrates this concept. The voxel model has also been transferred to a conventional triangulated surface parameterization in STL format[3] given in Fig. 41, which gives a clear image of the geometry.

---

[2] Courtesy of IZFP Fraunhofer Institute for Non-Destructive Testing, Saarbrücken, Germany; http://www.izfp.fraunhofer.de.

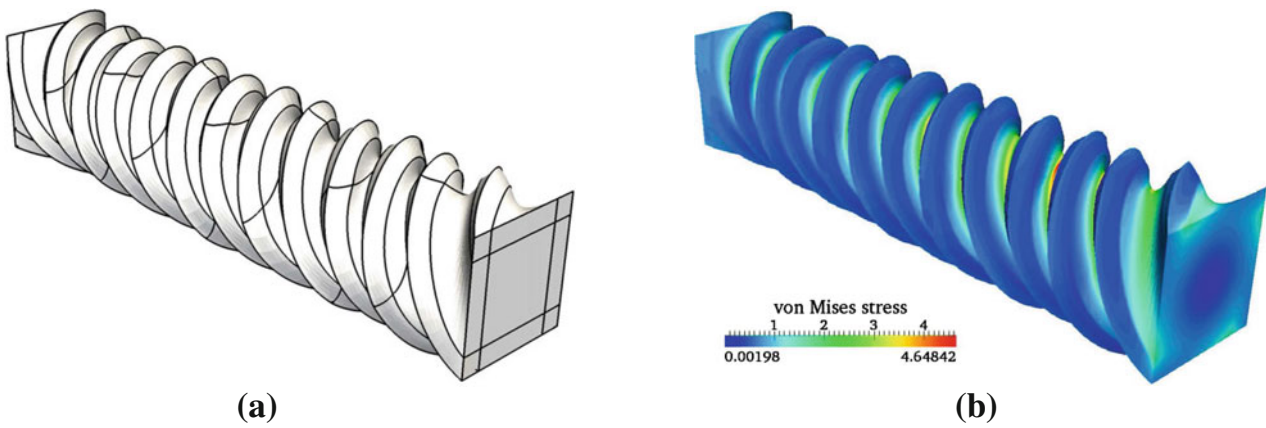[3] Surface Tesselation Language, also Standard Triangulation Language.

Fig. 36 The beam under an extreme rotation of $\theta = 1,080°$, computed with the p-version of the FCM. **a** Deformed p-version cell mesh in the physical domain. The fictitious domain part is cut away, **b** Von Mises stress plotted on the deformed configuration
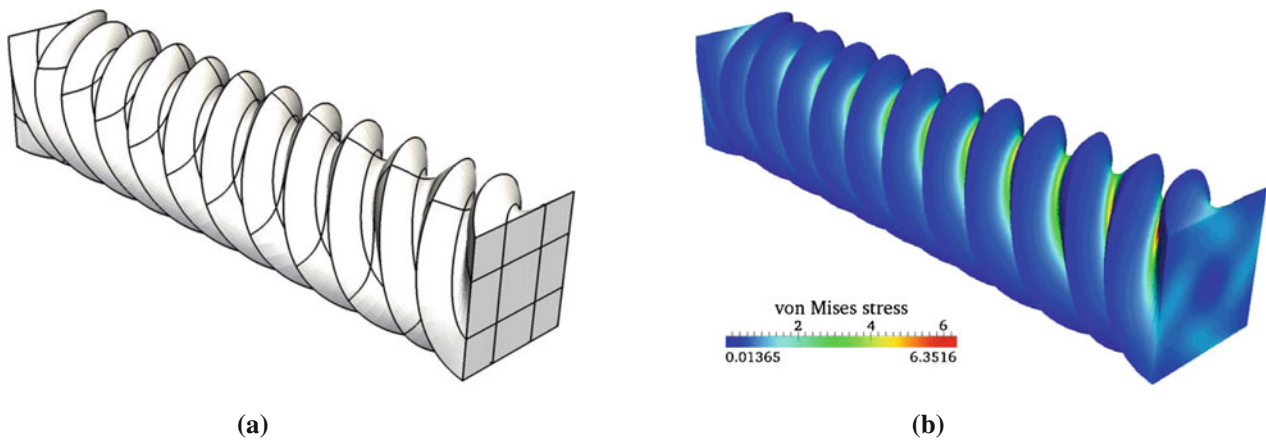

Fig. 37 The beam under an extreme rotation of $\theta = 1,080°$, computed with the B-spline version of the FCM. **a** Deformed knot span cell mesh in the physical domain. The fictitious domain part is cut away, **b** Von Mises stress plotted on the deformed configuration

With the help of the bit code, an adaptive integration structure that decomposes finite cells cut by geometric boundaries into sub-cells to accurately take into account the discontinuity in α (see Sect. 2.2), can then be established by the following simple algorithm

1. Traverse all sub-cells of the currently finest level k (start with the finite cells at $k = 0$) and query each Gauss point if it is in Ω_{phys} or Ω_{fict}.
2. If Gauss points of the same sub-cell are located in different domains (hence, a geometric boundary must be present), split the sub-cell into sub-cells of the next level $k = k + 1$.
3. Provide all new sub-cells with $(p + 1)^n$ Gauss points, where n denotes the number of Cartesian directions.
4. Repeat this process, until a sufficient sub-cell depth $k = m$ is reached.

The voxel-based bit code provides an ideal geometrical basis for the corresponding location query, which determines for an arbitrary point in space, if it is located in the physical or fictitious domain. Assuming a lexicographical ordering of the voxel data, the integration point position $\{X, Y, Z\}^T$ in the reference configuration can be related to the voxel index k_{vox} with corresponding b_{vox} by

$$k_{vox} = \left\lfloor \frac{(X - X_0)\, n_x}{L_x} \right\rfloor n_y n_z + \left\lfloor \frac{(Y - Y_0)\, n_y}{L_y} \right\rfloor n_z + \left\lfloor \frac{(Z - Z_0)\, n_z}{L_z} \right\rfloor + 1 \tag{62}$$

where $\{X_0, Y_0, Z_0\}$, $\{L_x, L_y, L_z\}$ and $\{n_x, n_y, n_z\}$ denote the origin, the length and the number of voxels in each Cartesian direction, and $\lfloor \ \rfloor$ is the floor function.

To illustrate the efficiency of the algorithm, the voxel-based geometry of the metal foam shown in Fig. 40 is discretized with $5 \times 5 \times 5$ p-version finite cells of polynomial

Fig. 38 Deformed finite cell mesh including the fictitious domain for a beam rotation of $\theta = 180°$. **a** Deformed p-version cells of Fig. 32a, **b** deformed knot span cells of Fig. 32b

(a)   (b)

Size of the physical part of the mesh

Physical part of the mesh

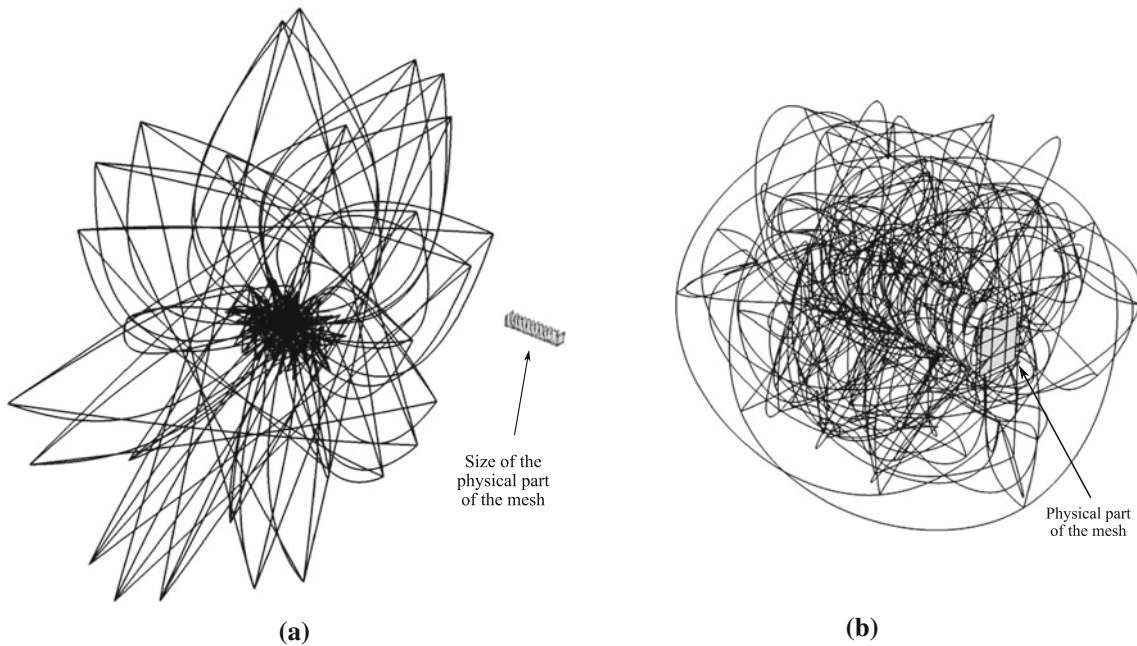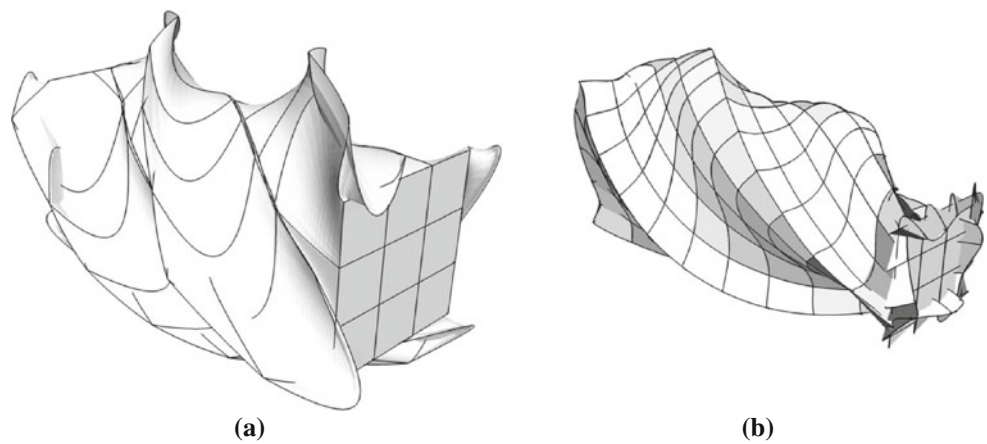(a)   (b)

Fig. 39 Deformed finite cell mesh including the fictitious domain for a beam rotation of $\theta = 1,080°$, given by the contours of the cell faces covering the fictitious domain. The deformed physical part of the meshes shown in Figs. 36a and 37a are also plotted to give an idea of the size of the deformation of the fictitious domain. **a** Deformed p-version cells, **b** deformed knot span cells

degree $p = 7$ and $m = 3$ levels of adaptive sub-cells. The fully automated generation of the corresponding discretization shown in Fig. 42 can be accomplished in only 42 seconds.[4] The main costs result from the loading of voxel information encoded by approximately 10^9 (1 billion) bits, the generation of 25,247 adaptive sub-cells and about 680,000 integration point queries according to Eq. 62. It can be easily observed that the adaptive aggregation of sub-cells around geometric boundaries increases quickly with k.

9.2 Large deformation analysis of an open-cell aluminium foam

Metal foams provide high stiffness at reduced weights, and are therefore frequently used for lightweight structures in automotive and aerospace applications [90]. The p- and B-spline versions of the FCM are applied to simulate a compression test for an aluminium foam sample of size $20 \times 20 \times 20$ mm. Its internal geometry is provided by voxels with a resolution of 1024^3 in each Cartesian direction, each of which encodes α. Figure 40b shows all voxels of material index 1 associated with aluminium in a coarsened resolution of 128^3.

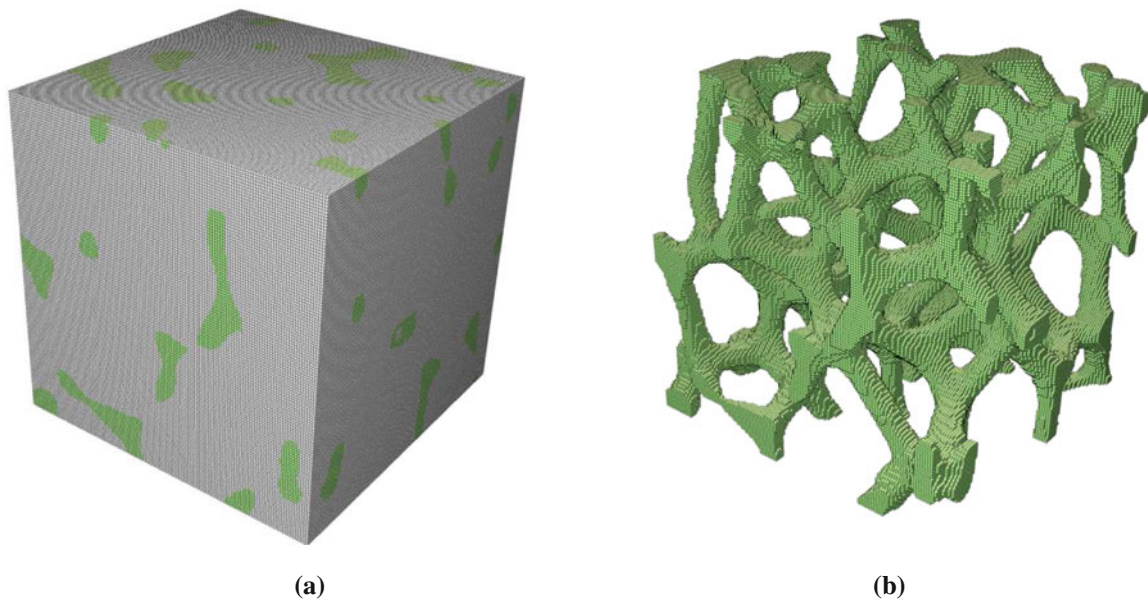[4] On a Intel(R) Core(TM)2 P8800 @ 2.66 GHz.

Fig. 40 CT-based voxel model of an aluminium foam sample. For better visibility, the original resolution of 1024^3 voxels is reduced to 128^3. **a** Voxelized sample cube, **b** voxels with $b_{vox} = 1$
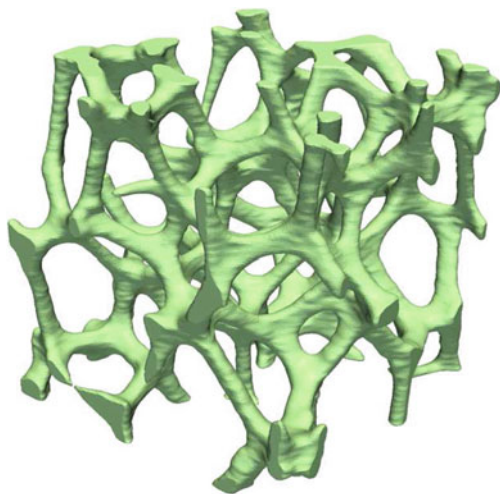

Fig. 41 STL surface parameterization

The foam sample is assumed as part of a larger specimen, which is uniformly compressed along the vertical axis. A corresponding RVE[5] model [78,91] specifies boundary conditions as follows: displacements normal to the top surface are gradually increased to 1.6 mm (8% compressive deformation), modelling the influence of a testing machine, whereas the displacements normal to all other surfaces are fixed due to the bottom support and the influence of the surrounding material of the specimen. Since Dirichlet boundaries coincide with cell faces, Dirichlet constraints are imposed strongly. The aluminium foam is characterized by Young's modulus

$E = 70.000$ N/mm^2, penalized by $\alpha = 10^{-12}$ at all integration points in Ω_{fict}, and Poisson's ratio $\nu = 0.35$. For the p-version of the FCM, the discretization shown in Fig. 42 is used, while the B-spline version discretizes the sample with $12 \times 12 \times 12$ knot span cells and $m = 2$ levels of adaptive sub-cells. Thus, the smallest sub-cells of the p-version and B-spline discretizations, respectively, contain approx. 25 and 21 voxels in each direction.

Our in-house FCM code implements both FCM versions in the same framework based on Sandia's library package Trilinos [81], the direct solver Lapack [92] and parallelization with OpenMP [93], where the same routines are applied for linear algebra operations, adaptive integration, the linear elastic material, assembly of the stiffness matrix and the Newton–Raphson iterative procedure, and the only difference consists of the numbering and evaluation of the shape functions. For the p-version mesh (21,492 dofs; 24,947 sub-cells; approx. 12.75 million Gauss points), analysis of the foam could be accomplished by our in-house FCM code in about 4 h,[6] whereas the B-spline mesh (18,411 dofs; 37,414 sub-cells; approx. 19.16 million Gauss points) took about 9.5 h. Since the major cost of FCM results from integration of the large number of sub-cells with $(p + 1)$ Gauss points in each local direction, a major performance gain is achieved by the shared memory parallelization of the loop that computes local stiffness matrices for cells and sub-cells with subsequent assembly into the global system matrix. A

---

[5] Representative volume element.

[6] Using 8 threads on 2 interconnected Intel(R) Xeon(R) W5590 @ 3.33 GHz with 70 GB RAM.
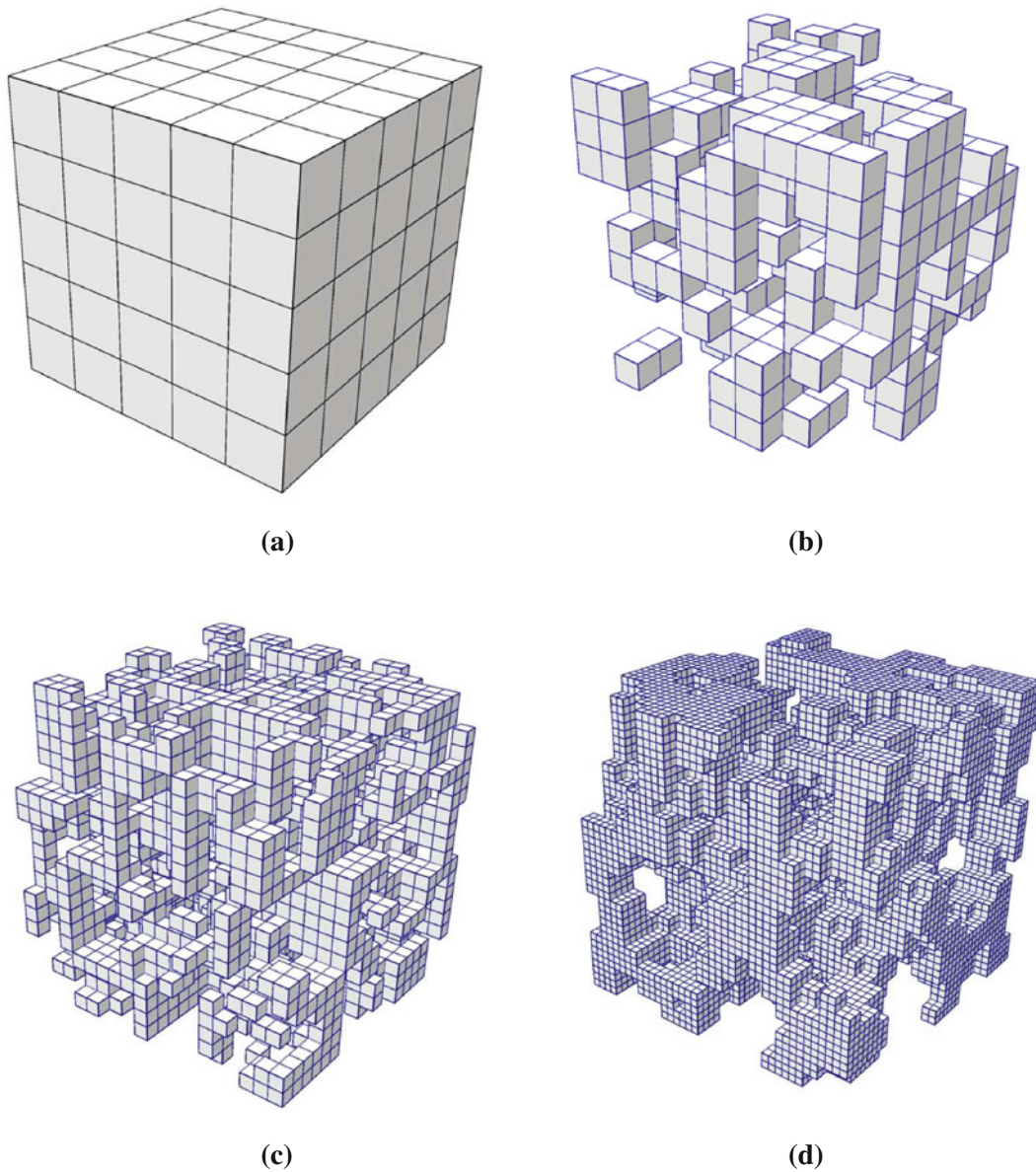
(a)

(b)

(c)

(d)

Fig. 42 Discretization of the metal foam sample with the *p*-version of the FCM with $m = 3$ levels of sub-cells, each with $(p + 1)^3$ Gauss points, leading to an adaptive aggregation of integration points around geometric boundaries. **a** Structured high-order mesh ($k = 0$), consisting of 125 *p*-version finite cells, **b** first level $k = 1$ of the adaptive integration structure, consisting of 306 sub-cells, **c** second level $k = 2$ of the adaptive integration structure, consisting of 2,197 sub-cells, **d** third level $k = 3$ of the adaptive integration structure, consisting of 22,744 sub-cells

parallel for construct creates a team of *n* threads to execute the main loop over sub-cells in parallel, where *n* is the number of threads available. With $n = 8$, we achieved a strong speed up of the loop of around 5.

The resulting von Mises stresses computed with the *p*- and B-spline versions at $p = 7$ are shown in Fig. 43a, b, respectively. They exhibit accurate localization of stress concentrations at the convex sides of the foam members, which agrees well with engineering experience. Both plots show good accordance in terms of stress patterns, absolute

values and locations of stress peaks. Both discretizations converge in three load increments with 4–5 Newton iterations to a L^2-norm of the residual below 10^{-6}. Figure 44a plots the equivalent force obtained from integration of the normal stress over the top surface versus the prescribed displacement of the top surface for different polynomial degrees *p*, computed with the *p*-version mesh of Fig. 42. It can be observed that the increase of *p* improves the reproduction of the geometrically nonlinear behavior of the foam. Figure 44b illustrates the convergence of the equivalent top force under
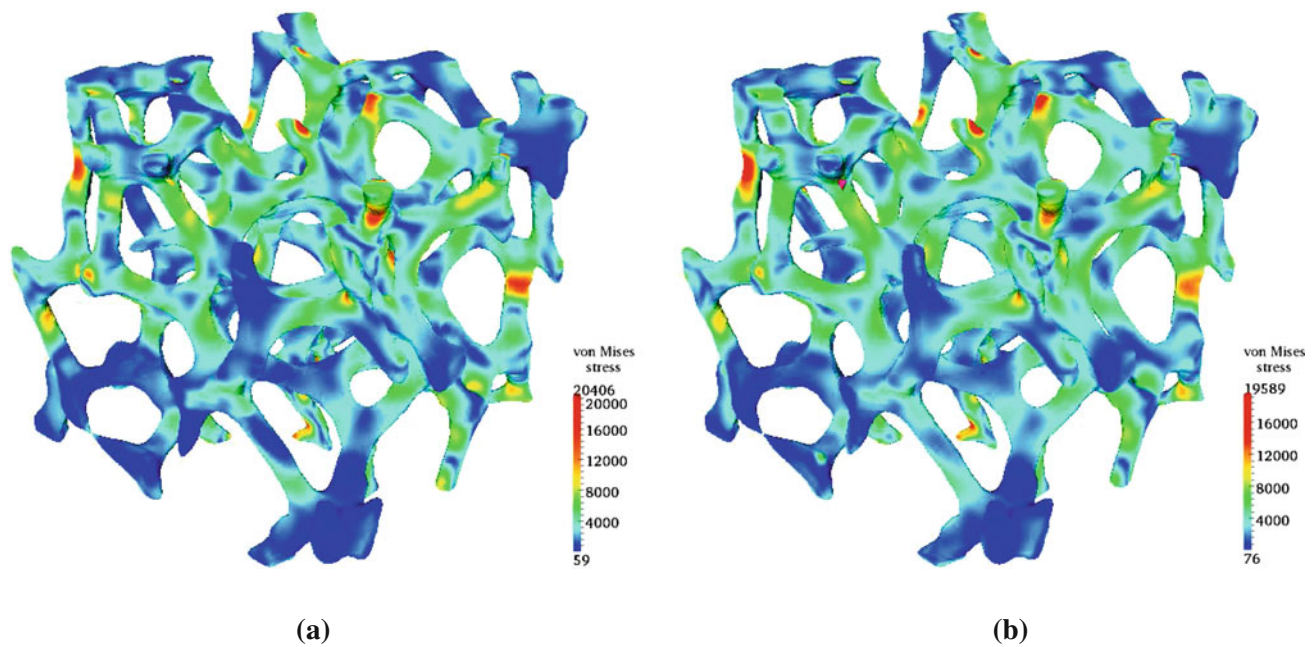
(a)　　　　　　　　　　　　　　　　　　　　**(b)**

Fig. 43 Von Mises stress of the metal foam sample plotted on the deformed configuration. The results are obtained from the FCM discretizations of polynomial degree $p = 7$ as described above. **a** p-version and **b** B-spline version of the FCM

p-refinement, obtained with the p- and B-spline versions of the FCM. Both schemes converge towards a final load of around 54 kN, where the B-spline discretization achieves a comparable accuracy with less degrees of freedom.

10 Comparison of the p- and B-spline versions of the Finite Cell Method

The numerical examples presented in this article clearly demonstrate that basis functions of the p-version of the FEM and high-order B-splines are both well-suited for the application in the framework of the generalized Finite Cell concept. Apart from the general validity of both approaches, a more detailed assessment of the benchmark tests of Sects. 7 and 8 as well as the application oriented examples of Sects. 3.3 and 9 reveals that each of the two methods has its specific strengths, which are briefly highlighted in the following.

Comparing p- and B-spline discretizations of the same polynomial degree p with a comparable amount of degrees of freedom, the *p-version of the FCM* has advantages in terms of computational efficiency. Hierarchic shape functions of the p-version are defined over only a few adjacent cells as opposed to B-splines, which are supported by a much larger number of knot spans due to their piecewise definition. This results in a smaller number of cells necessary to achieve the same amount of degrees of freedom and a higher degree of adaptivity of the integration sub-cells, which can be clearly

observed for example in the p-version and B-spline discretizations shown in Fig. 11. A further consequence is a smaller degree of population of the stiffness matrix in the p-version of the FCM, in particular for high-order computations in 3D. The combination of less sub-cells at a comparable resolution of geometric boundaries and smaller degree of population at the same polynomial degree makes the p-version of the FCM computationally more efficient than the B-spline version, as illustrated by the computational times given in Sect. 9 for the foam example.

The *B-spline version of the FCM* has advantages in terms of accuracy. Due to the smooth extension of solution fields into the fictitious domain, the FCM can make use of the higher-order continuity of the B-spline basis. In contrast, the p-version basis is only C^0-continuous along cell boundaries, and therefore leads to discontinuities in stresses. Consequently, the p-version basis can be considered richer than actually required by the target solution, for which a best approximation in terms of the strain energy is to be found. Therefore, the smooth approximation space of the B-spline version can achieve the same level of accuracy with less degrees of freedom than the p-version of the FCM, which "wastes" part of its approximation power to unnecessary solution components. This characteristic feature can be observed in the strain energy results of the benchmark examples presented in Sect. 7, in particular for the cube with a spherical hole, as well as in the application related examples of the proximal femur bone of Sect. 3.3 and the
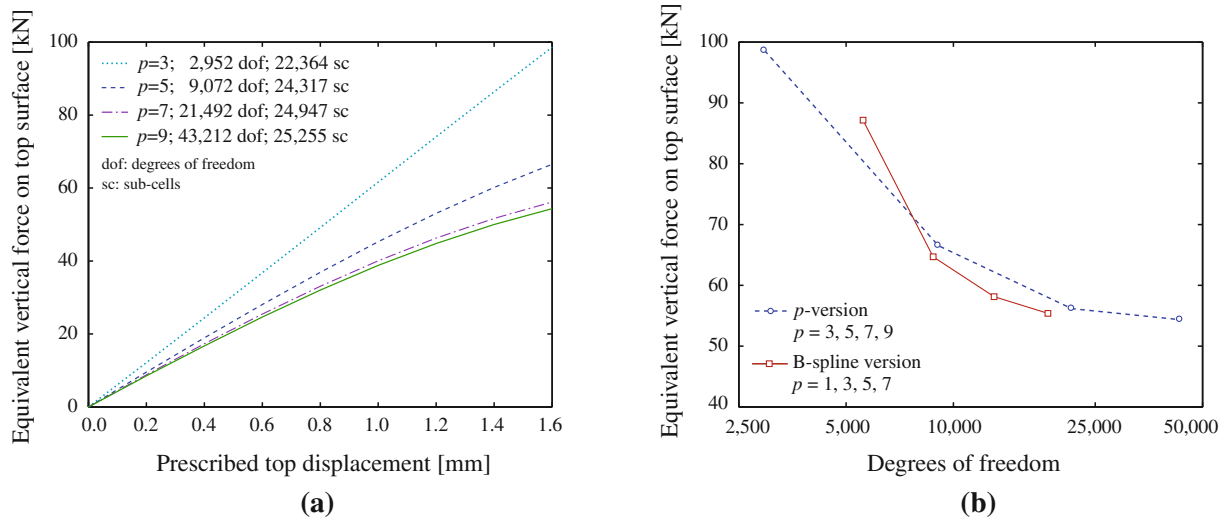
Fig. 44 Convergence behavior under *p*-refinement for the given *p*- and B-spline discretizations of the foam sample. **a** Force–displacement behavior with increasing *p*, obtained from the discretization given in Fig. 42, **b** convergence of the equivalent vertical force for the *p*- and B-spline versions of the FCM

metal foam of Sect. 9. It partly compensates the efficiency drawback in comparison to the *p*-version described above. The beam under very large torsion presented in Sect. 8 indicated that C^0-continuous *p*-version cells show some advantages over higher-order continuity B-spline cells in the presence of extremely large deformations, since they permit a greater freedom for solution fields in the fictitious domain.

11 Summary and conclusions

The article at hand deals with two main new aspects: the application of high-order and high-continuity B-spline bases within the FCM and the extension of the FCM concept to geometrically nonlinear problems. First, a review of the basic ingredients of the generalized FCM concept was provided, i.e. the fictitious domain idea, a structured grid of high-order elements, adaptive integration of geometric boundaries, weak imposition of unfitted Dirichlet boundary conditions. The *p*-version and B-spline bases were introduced as examples of suitable high-order Ansatz spaces, which successfully instantiate the characteristic FCM properties, i.e. easy mesh generation irrespective of the geometric complexity involved and exponential rates of convergence under *p*-refinement. The corresponding FCM schemes were coined the *p*- and B-spline versions of the FCM. Considering several linear elastic examples, it was shown that for small deformation analysis, both FCM versions provide a comparable overall solution behavior in conjunction with Nitsche's method and for a complex three-dimensional proximal femur bone with inhomogeneous material parameters.

Both FCM versions were then combined with standard finite element technology for large deformation analysis, based on geometrically nonlinear elasticity in principal directions. It was shown that a standard geometrically nonlinear FCM formulation, using the same kinematics over the complete domain, leads to the loss of uniqueness of the deformation map in the fictitious domain. A stabilization can be achieved by increasing the penalty parameter, which in turn provokes a larger modeling error and excessive stress oscillations in cells cut by geometric boundaries. This motivated a modified FCM formulation, based on repeated deformation resetting, which assumes for the fictitious domain the deformation-free reference configuration after each Newton iteration. Thus, the stability issue in the fictitious domain can be completely circumvented, since the deformation map and related quantities are inherently known and do not need to be computed. In particular, the deformation resetting is equivalent to performing repeated linear analyses in the fictitious domain, which considerably reduces the computational cost. In addition, the consistent linearization of the penalty method was derived and integrated into the modified FCM formulation for the imposition of unfitted Dirichlet boundary conditions in the geometrically nonlinear context.

It was demonstrated by a range of numerical experiments in one, two and three dimensions that the modified formulation allows for stable FCM analysis with both the *p*- and B-spline versions, while preserving the accuracy, physical consistency and exponential rates of convergence of the geometrically nonlinear solution within the physical domain. It was furthermore demonstrated that both FCM versions inherit the robustness of the corresponding high-order basis. They proved to be able to accurately represent very large

deformation states despite the presence of the fictitious domain and severe distortion of the physical parts of the FCM meshes. The capability of the FCM to directly operate on voxel-based geometrical models without any pre-processing, segmentation of the voxel data or time-consuming mesh generation was illustrated by the large deformation analysis of a CT-based metal foam sample. A *p*-refinement study, the accurate localization of stress peaks and the good accordance of *p*-version and B-spline results corroborated the high accuracy of the foam analysis. While the overall solution characteristics were found to be equivalent, a detailed comparison revealed specific strengths of each FCM version: for knot span and *p*-version discretizations with a comparable number of degrees of freedom, the B-spline version tends to yield more accurate results due to the higher-order continuity of its basis. The *p*-version tends to be computationally more efficient due to a lower degree of population and bandwidth of the stiffness matrix.

Based on these results, we believe that both FCM versions have great potential for the accurate analysis of very complex geometries, and a plethora of very promising aspects are still open, such as the analysis of topology changes and moving boundaries, for which embedded domain methods such as the FCM offer significant advantages over ALE-type approaches, or the introduction of FCM suitable coupling schemes for multiphysics problems, which stand at the forefront of today's challenges in computational science.

References

1. Bathe K-J (1996) Finite element procedures. Prentice Hall, Upper Saddle River
2. Hughes TJR (2000) The finite element method: linear static and dynamic finite element analysis. Dover, New York
3. Hughes TJR, Cottrell JA, Bazilevs Y (2005) Isogeometric analysis: CAD, finite elements, NURBS, exact geometry and mesh refinement. Comput Methods Appl Mech Eng 194:4135–4195
4. Cottrell JA, Hughes TJR, Bazilevs Y (2009) Isogeometric analysis: toward integration of CAD and FEA. Wiley, New York
5. Bazilevs Y, Calo VM, Cottrell JA, Evans JA, Hughes TJR, Lipton S, Scott MA, Sederberg TW (2010) Isogeometric analysis using T-splines. Comput Methods Appl Mech Eng 199:229–263
6. Neittaanmäki P, Tiba D (1995) An embedding domains approach in free boundary problems and optimal design. SIAM Control Optim 33(5):1587–1602
7. Peskin C (2002) The immersed boundary method. Acta Numer 11:1–39
8. Mittal R, Iaccarino G (2005) Immersed boundary methods. Ann Rev Fluid Mech 37:239–261
9. Löhner R, Cebral RJ, Camelli FE, Appanaboyina S, Baum JD, Mestreau EL, Soto OA (2008) Adaptive embedded and immersed unstructured grid techniques. Comput Methods Appl Mech Eng 197:2173–2197
10. Del Pino S, Pironneau O (2003) A fictitious domain based general PDE solver. In: Kuznetsov Y, Neittanmäki P, Pironneau O (eds) Numerical methods for scientific computing: variational problems and applications. CIMNE, Barcelona
11. Glowinski R, Kuznetsov Y (2007) Distributed Lagrange multipliers based on fictitious domain method for second order elliptic problems. Comput Methods Appl Mech Eng 196:1498–1506
12. Ramière I, Angot P, Belliard M (2007) A fictitious domain approach with spread interface for elliptic problems with general boundary conditions. Comput Methods Appl Mech Eng 196:766–781
13. Bishop J (2003) Rapid stress analysis of geometrically complex domains using implicit meshing. Comput Mech 30:460–478
14. Baaijens FPT (2001) A fictitious domain/mortar element method for fluid-structure interaction. Int J Numer Methods Fluids 35:743–761
15. Farhat C, Hetmaniuk U (2002) A fictitious domain decomposition method for the solution of partially axisymmetric acoustic scattering problems. Part I: Dirichlet boundary conditions. Int J Numer Methods Eng 54:1309–1332
16. Haslinger J, Kozubek T, Kunisch K, Peichl G (2003) Shape optimization and fictitious domain approach for solving free boundary problems of bernoulli type. Comput Optim Appl 26:231–251
17. Burman E, Hansbo P (2010) Fictitious domain finite element methods using cut elements: I. A stabilized Lagrange multiplier method. Comput Methods Appl Mech Eng 199:2680–2686
18. Gerstenberger A, Wall WA (2010) An embedded Dirichlet formulation for 3D continua. Int J Numer Methods Eng 82:537–563
19. Burman E, Hansbo P (2011) Fictitious domain finite element methods using cut elements: II. A stabilized Nitsche method. Appl Numer Math. doi:10.1016/j.apnum.2011.01.008
20. Sukumar N, Chopp DL, Moës N, Belytschko T (2001) Modeling holes and inclusions by level sets in the extended finite-element method. Comput Methods Appl Mech Eng 190:6183–6200
21. Gerstenberger A, Wall WA (2008) An eXtended Finite Element Method/Lagrange multiplier based approach for fluid-structure interaction. Comput Methods Appl Mech Eng 197:1699–1714
22. Haslinger J, Renard Y (2009) A new fictitious domain approach inspired by the extended finite element method. SIAM J Numer Anal 47:1474–1499
23. Becker R, Burman E, Hansbo P (2011) A hierarchical NXFEM for fictitious domain simulations. Int J Numer Methods Eng 86(4–5):54–559
24. Bastian P, Engwer C (2009) An unfitted finite element method using discontinuous Galerkin. Int J Numer Methods Eng 79:1557–1576
25. Legay A, Wang HW, Belytschko T (2005) Strong and weak arbitrary discontinuities in spectral finite elements. Int J Numer Methods Eng 64:991–1008
26. Lui S (2009) Spectral domain embedding for elliptic PDEs in complex domains. J Comput Appl Math 225:541–557
27. Parussini L, Pediroda V (2009) Fictitious domain approach with *hp*-finite element approximation for incompressible fluid flow. J Comput Phys 228:3891–3910
28. Parvizian J, Düster A, Rank E (2007) Finite Cell Method: *h*- and *p*-extension for embedded domain methods in solid mechanics. Comput Mech 41:122–133
29. Düster A, Parvizian J, Yang Z, Rank E (2008) The Finite Cell Method for three-dimensional problems of solid mechanics. Comput Methods Appl Mech Eng 197:3768–3782
30. Szabó B, Babuška I (1991) Finite element analysis. Wiley, New York

31. Szabó B, Düster A, Rank E (2004) The *p*-version of the finite element method. In: Stein E, de Borst R, Hughes TJR (eds) Encyclopedia of computational mechanics, vol 1. Wiley, Chichester, pp 119–139

32. Rank E, Düster A, Schillinger D, Yang Z (2009) The Finite Cell Method: high order simulation of complex structures without meshing. In: Yuan Y, Cui J, Mang H (eds) Computational structural engineering. Springer, Heidelberg pp 87–92

33. Ruess M, Tal D, Trabelsi N, Yosibash Z, Rank E (2011) The Finite Cell Method for bone simulations: verification and validation. Biomech Model Mechanobiol. doi:10.1007/s10237-011-0322-2

34. Schillinger D, Düster A, Rank E (2011) The *hp-d* adaptive Finite Cell Method for geometrically nonlinear problems of solid mechanics. Int J Numer Methods Eng. doi:10.1002/nme.3289

35. Vos PEJ, van Loon R, Sherwin SJ (2008) A comparison of fictitious domain methods appropriate for spectral/*hp* element discretisations. Comput Methods Appl Mech Eng 197:2275–2289

36. Parvizian J, Düster A, Rank E (2011) Topology optimization using the Finite Cell Method. Opt Eng. doi:10.1007/s11081-011-9159-x

37. Rank E, Kollmannsberger S, Sorger C, Düster A (2011) Shell Finite Cell Method: a high order fictitious domain approach for thin-walled structures. Comput Methods Appl Mech Eng 200:3200–3209

38. Vinci C (2009) Application of Dirichlet boundary conditions in the Finite Cell Method. Master thesis, Lehrstuhl für Computation in Engineering, Technische Universität München

39. Zander N (2011) The Finite Cell Method for linear thermoelasticity. Master thesis, Lehrstuhl für Computation in Engineering, Technische Universität München

40. Abedian A, Parvizian J, Düster A, Khademyzadeh H, Rank E (2010) The Finite Cell Method for elasto-plastic problems. In: Proceedings of the 10th international conference on computational structures technology, Valencia, 2010

41. Cai Q, Kollmannsberger S, Mundani RP, Rank E (2011) The Finite Cell Method for solute transport problems in porous media. In: Proceedings of the 16th international conference on finite elements in flow problems, Munich, 2011

42. Düster A, Sehlhorst HG, Rank E (2012) Numerical homogenization of heterogeneous and cellular materials utilizing the Finite Cell Method. Comp Mech. doi:10.1007/s00466-012-0681-2

43. Yang Z, Ruess M, Kollmannsberger S, Düster A, Rank E (2012) An efficient integration technique for the voxel-based Finite Cell Method. Int J Numer Methods Eng (accepted)

44. Allaire G, Jouve F, Toader A (2004) Structural optimization using sensitivity analysis and a level-set method. J Comput Phys 194:363–393

45. Bonet J, Wood R (2008) Nonlinear continuum mechanics for finite element analysis. Cambridge University Press, Cambridge

46. Sueli E, Mayers DF (2003) An introduction to numerical analysis. Cambridge University Press, Cambridge

47. Samet H (2006) Foundations of multidimensional and metric data structures. Morgan Kaufmann Publishers, San Francisco

48. Zohdi T, Wriggers P (2001) Aspects of the computational testing of the mechanical properties of microheterogeneous material samples. Int J Numer Methods Eng 50:2573–2599

49. Düster A (2001) High order finite elements for three-dimensional, thin-walled nonlinear continua. PhD thesis, Lehrstuhl für Bauinformatik, Technische Universität München, Shaker, Aachen

50. Düster A, Bröker H, Rank E (2001) The *p*-version of the finite element method for three-dimensional curved thin walled structures. Int J Numer Methods Eng 52:673–703

51. Schillinger D, Kollmannsberger S, Mundani R-P, Rank E (2010) The Finite Cell Method for geometrically nonlinear problems of solid mechanics. IOP Conf Ser Mater Sci Eng 10:012170

52. Schillinger D, Rank E (2011) An unfitted *hp*-adaptive finite element method based on hierarchical B-splines for interface problems of complex geometry. Comput Methods Appl Mech Eng 200(47–48):3358–3380

53. Piegl LA, Tiller W (1997) The NURBS book (monographs in visual communication). Springer, New York

54. Rogers DF (2001) An introduction to NURBS with historical perspective. Morgan Kaufmann Publishers, San Francisco

55. Höllig K (2003) Finite element methods with B-splines. Society for Industrial and Applied Mathematics, Philadelphia

56. Babuška I (1972) The finite element method with penalty. Math Comput 27(122):221–228

57. Zhu T, Atluri SN (1998) A modified collocation method and a penalty formulation for enforcing the essential boundary conditions in the element free Galerkin method. Comput Mech 21:211–222

58. Babuška I, Banerjee U, Osborn JE (2002) Meshless and generalized finite element methods: a survey of some major results. In: Griebel M, Schweitzer MA (eds) Meshfree methods for partial differential equations. Lecture notes in computational science and engineering, vol 26. Springer, Berlin

59. Fernandez-Mendez S, Huerta A (2004) Imposing essential boundary conditions in mesh-free methods. Comput Methods Appl Mech Eng 193:1257–1275

60. Zienkiewicz OC, Taylor RL (2005) The finite element method vol 1: the basis. Butterworth-Heinemann, Oxford

61. Hansbo A, Hansbo P (2002) An unfitted finite element method, based on Nitsche's method, for elliptic interface problems. Comput Methods Appl Mech Eng 191:537–552

62. Bazilevs Y, Hughes TJR (2007) Weak imposition of Dirichlet boundary conditions in fluid mechanics. Comput Fluids 36: 12–26

63. Embar A, Dolbow J, Harari I (2010) Imposing Dirichlet boundary conditions with Nitsche's method and spline-based finite elements. Int J Numer Methods Eng 83:877–898

64. Harari I, Dolbow J (2010) Analysis of an efficient finite element method for embedded interface problems. Comput Mech 46:205–211

65. Sadd MH (2009) Elasticity: theory, applications, and numerics. Academic Press, Oxford

66. Keyak J, Falkinstein Y (2003) Comparison of in situ and in vitro CT-scan-based finite element model predictions of proximal femoral fracture load. J Med Eng Phys 25:781–787

67. Schileo E, Dall'Ara E, Taddei F, Malandrino A, Schotkamp T, Viceconti M (2008) An accurate estimation of bone density improves the accuracy of subject-specific finite element models. J Biomech 41:2483–2491

68. Bungartz HJ, Griebel M, Zenger C (2004) Introduction to computer graphics. Charles River Media, Hingham

69. Novelline R (1997) Squire's fundamentals of radiology. Harvard University Press, Cambridge

70. Yosibash Z, Padan R, Joskowicz L, Milgrom C (2007) A CT-based high-order finite element analysis of the human proximal femur compared to in-vitro experiments. J Biomech Eng 129:297–309

71. Trabelsi N, Yosibash Z, Milgrom C (2009) Validation of subject-specific automated *p*-FE analysis of the proximal femur. J Biomech 42:234–241

72. Belytschko T, Liu WK, Moran B (2006) Nonlinear finite elements for continua and structures. Wiley, New York

73. de Souza Neto EA, Perić D, Owen DRJ (2008) Computational methods for plasticity: theory and applications. Wiley, New York

74. Wriggers P (2008) Nonlinear finite element methods. Springer, Berlin

75. Holzapfel G (2000) Nonlinear solid mechanics. A continuum approach for engineering. Wiley, New York

76. Noël AT, Szabó B (1997) Formulation of geometrically non-linear problems in the spatial reference frame. Int J Numer Methods Eng 40:1263–1280

77. Düster A, Hartmann S, Rank E (2003) *p*-FEM applied to finite isotropic hyperelastic bodies. Comput Methods Appl Mech Eng 192:5147–5166

78. Sehlhorst HG, Jänicke R, Düster A, Rank E, Steeb H, Diebels S (2009) Numerical investigations of foam-like materials by nested high-order finite element methods. Comput Mech 45:45–59

79. Krause R, Mücke R, Rank E (1995) *hp*-version finite elements for geometrically non-linear problems. Commun Numer Methods Eng 11:887–897

80. Bertsekas DP (1996) Constrained optimization and lagrange multiplier methods. Athina Scientific, Nashua

81. Trilinos Version 10.4, Sandia National Laboratories, Los Alamos, NM. http://trilinos.sandia.gov/

82. MKL PARDISO. www.intel.com/software/products/mkl. 16 January 2012

83. FlagShyp 08 Version 2.30, Nonlinear FE solver developed by J. Bonet and R. Wood. http://www.flagshyp.com

84. Visual DoMesh 2008 Version 1.1, Mesh generator developed by C. Sorger, Chair for Computation in Engineering, Technische Universität München

85. Netgen Version 4.9.13, Tetrahdral mesh generator developed by J. Schöberl. http://sourceforge.net/projects/netgen-mesher

86. ParaView Version 3.8.1, Open-source scientific visualization package. Kitware Inc., Clifton Park, NY. http://www.paraview.org

87. Dong S, Yosibash Z (2009) A parallel spectral element method for dynamic three-dimensional nonlinear elasticity problems. Comput Struct 87(1–2):59–72

88. Elguedj T, Bazilevs Y, Calo VM, Hughes TJR (2008) B-bar and F-bar projection methods for nearly incompressible linear and nonlinear elasticity and plasticity using higher-order NURBS elements. Comput Methods Appl Mech Eng 197:2732–2762

89. Lipton S, Evans JA, Bazilevs Y, Elguedj T, Hughes TJR (2010) Robustness of isogeometric structural discretizations under severe mesh distortion. Comput Methods Appl Mech Eng 199:357–373

90. Banhart J (2001) Manufacture, characterization and application of cellular metals and metal foams. Prog Mater Sci 46:559–632

91. Zohdi T, Wriggers P (2005) Introduction to computational micromechanics. Springer, Berlin

92. Lapack Version 3.2.2. (2010) Linear algebra package. http://www.netlib.org/lapack/

93. Chapman B, Jost G, van der Pas R (2008) Using OpenMP. Portable shared memory parallel programming. MIT Press, Cambridge